Tropospheric Emission Spectrometer (TES) Spectrum Reconstruction Analysis Summary

Andre Tkacenko*, Matthew D. Thill*, and Curtis Jin†

ABSTRACT. — The purpose of this article is to summarize the attempts made to carry out spectrum reconstruction for interferograms obtained from the Tropospheric Emission Spectrometer (TES) on-board the Aura satellite, after the laser used to trigger the sampling unit malfunctioned in the spring of 2016. In particular, we highlight the drawbacks that made reconstruction problematic and the approaches attempted to overcome them. These drawbacks include ill-conditioning of the reconstruction problem incurred with nonuniformly spaced interferogram samples, discrepancies in the reported and true spatial locations of the samples, and low resolution of the spatial location data. Algorithms used to overcome these pitfalls, involving regularized reconstruction methods in the case of unknown/imperfect sample locations, are presented, along with reconstruction results showing the difficulties associated with the spectrum reconstruction problem.

I. Introduction

In the spring of 2016 until the early part of 2017, the laser from the Tropospheric Emission Spectrometer (TES) instrument on-board the Aura (EOS CH-1) NASA Earth observation satellite ceased to be operational. This laser was used as part of a Michelson interferometer to help generate samples of interferogram (IFGM) waveforms that were uniformly spaced in terms of optical path difference (OPD), as shown in Figure 1. Specifically, the laser was used to trigger the analog-to-digital converter (ADC) used to sample an IFGM waveform based on integer multiples of the laser fringe counts observed.

---

*Communications Architectures and Research Section.

†Flight Communications Systems Section.

The research described in this publication was carried out by the Jet Propulsion Laboratory, California Institute of Technology, under a contract with the National Aeronautics and Space Administration.

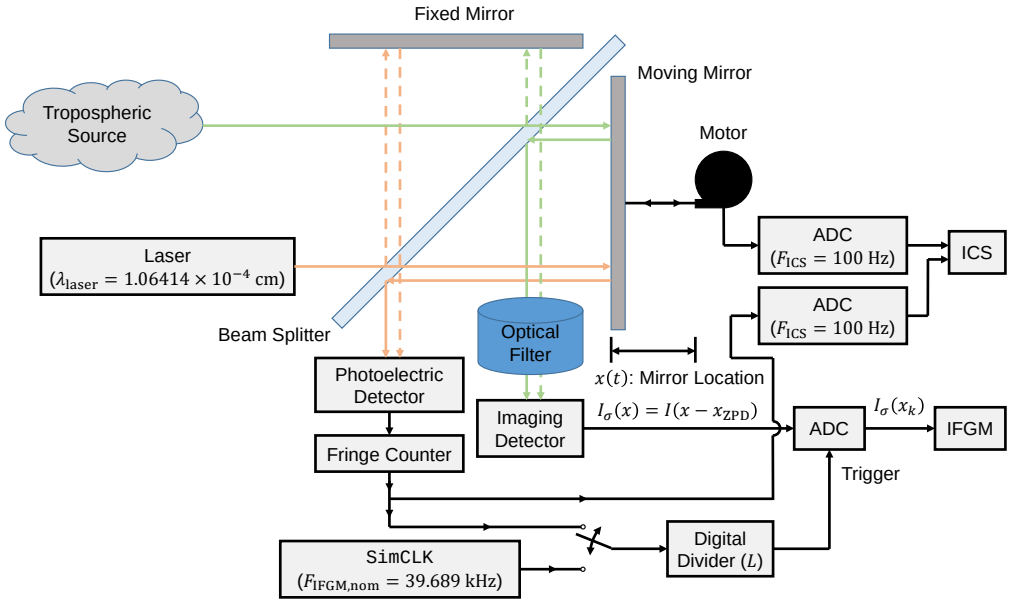

Figure 1. Block diagram of TES instrument setup.

In the event that the laser ceased to be operational, a backup system had been implemented in which IFGM samples from the ADC were collected uniformly in time. This system, referred to as the `SimCLK` module[1], generated roughly the same number of samples during a scan as the nominal laser setup. However, as the mirror in the Michelson interferometer does not move at a constant velocity, this resulted in IFGM samples that were, in general, nonuniformly spaced in terms of OPD.

In order to make the reconstruction of the desired IFGM spectrum even remotely feasible, the mapping of the mirror location (effectively the OPD) as a function of time had to be established. Information for this mapping was provided by the Instrument Control Subsystem (ICS) module within TES[2]. This subsystem provided mirror encoder position information, as well as fringe count values (valid when the laser was operational) at discrete values of time, from which an OPD time series could nominally be derived. However, samples from the ICS were generally at a much lower time resolution than those obtained for the IFGM waveform from `SimCLK`.

A. Outline

In Section II, we describe in detail the spectrum reconstruction problem encountered for TES. There, we show how the desired IFGM spectral values are related to the given OPD-domain IFGM samples. It is shown how the IFGM samples can be found

---

[1]K. W. Bowman, E. Sarkissian, D. Tremblay, H. M. Worden, and J. Zong, "*Tropospheric Emission Spectrometer (TES) Level 1 Algorithm Theoretical Basis Document*," Version 2.0, D-16479 (internal document), Jet Propulsion Laboratory, California Institute of Technology, Pasadena, CA, July 6, 2004.

[2]Ibid.

from the OPD-domain IFGM samples by solving an overdetermined linear system of equations.

In Sections III, IV, and V, we cover some of the obstacles encountered with respect to solving the spectrum reconstruction problem specifically for TES. These issues are discussed in order of how they manifested throughout the analysis conducted for this study. However, in terms of the challenges they posed to successfully solving the spectrum reconstruction problem, they are presented in ascending order of difficulty.

In particular, in Section III, we highlight the ill-conditioning of the spectrum reconstruction problem in the presence of nonuniformly spaced data characteristic of that encountered for TES. This analysis is presented assuming the OPD positions of the IFGM samples are known exactly.

In Section IV, we present some of the discrepancies found for the OPD locations from different OPD time series returned from the ICS. There, it is shown that the ICS time series data for the mirror location from Figure 1 can have a discrepancy on the order of 10^{-3} cm, a value which is approximately equal to the Nyquist sampling interval for a 1B2 type waveform [3].

In Section V, we investigate the largest obstacle to successfully solving the spectrum reconstruction problem for TES, namely the low resolution of the ICS OPD data measurements. Specifically, the OPD locations for the IFGM samples must be obtained by interpolating the OPD time series data from the ICS. However, as the ICS data are only reported at a low rate of 100 Hz, this results in an overabundance of OPD locations that must be interpolated between adjacent ICS data measurements. Reliance on this level of interpolation for the sampling of the real bandpass signals of interest is shown to be especially deleterious.

In Sections VI and VII, we describe some of the signal processing algorithms considered for this study to solve the spectrum reconstruction problem for TES. While these methods were ultimately unsuccessful here, they may have applications for reconstruction problems with less severe uncertainties.

In Section VI, we cover a Tikhonov regularized spectrum reconstruction algorithm that applies for the case of unknown/imperfect sample locations. Specifically, the spectrum and position vectors for the IFGM waveform are jointly optimized. After globally optimizing the spectrum vector by solving the normal equations, a gradient descent algorithm is developed to locally optimize the position vector.

In Section VII, we present a power spectral density reconstruction algorithm applicable for the case of unknown/imperfect sample locations. This method exploits the fact that all IFGM waveforms are essentially shifted autocorrelation signals, which greatly improves the conditioning of the spectrum reconstruction problem. The spectrum and position vectors are jointly optimized as before. After globally

---

[3] Ibid.

optimizing the spectrum vector by solving a convex quadratic programming problem, a gradient descent algorithm is developed to locally optimize the position vector.

Finally, concluding remarks are made in Section VIII. There, we reflect on the pitfalls encountered with respect to the spectrum reconstruction problem for TES, which ultimately led to the failure of the proposed algorithms considered to solve this problem. Approaches for future investigations, in order to make the problem more feasible, are also presented.

II. Spectrum Reconstruction Problem

Let $I(x)$ denote a desired IFGM signal as a function of the OPD x. Ideally, this waveform would be centered such that the zero path difference (ZPD) occurs at $x = 0$, however, in practice, this need not be the case. Instead we have access to a shifted version of the IFGM, specifically $I_\sigma(x) \triangleq I(x - x_{\text{ZPD}})$, where x_{ZPD} is the location of the ZPD. From $I_\sigma(x)$, we are interested in reconstructing the Fourier transform spectrum $S_\sigma(\nu)$, where ν is the wavenumber. (After reconstructing $S_\sigma(\nu)$, we can recover $S(\nu)$ using $S(\nu) = S_\sigma(\nu)\, e^{j2\pi\nu x_{\text{ZPD}}}$, a process referred to as phase alignment [4].)

The signal model used to represent the IFGM waveforms and associated spectra encountered in TES comes from [1]. In particular, all IFGM waveforms are assumed to be real and expressible in terms of a discrete Fourier series (DFS) representation [2]. Furthermore, due to the presence of optical bandpass filters on TES [5], all IFGMs are bandpass and confined to alias band regions. This is shown pictorially in Figure 2. Here, ν_0 is the alias band width, while ℓ is the alias number for the alias band. By constraining $S_\sigma(\nu)$ (and equivalently $S(\nu)$) to this region, theoretically the entire IFGM waveform $I_\sigma(x)$ (and equivalently $I(x)$) can be reconstructed by uniformly sampling $I_\sigma(x)$ at the Nyquist rate $2\nu_0$, i.e., by sampling at $x = \frac{k}{2\nu_0}$ for $k \in \mathbb{Z}$ [2]. Furthermore, as $I_\sigma(x)$ is assumed to have a DFS representation, reconstruction can be guaranteed by sampling at $x = \frac{k}{2\nu_0}$, where k spans a set of consecutive integers equal to the number of terms in the DFS representation.

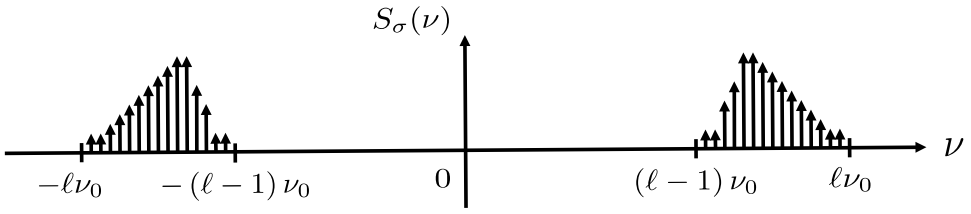

Figure 2. Graphical representation of bandpass IFGM spectrum $S_\sigma(\nu)$.

[4] Ibid.

[5] Ibid.

Let N_{spec} denote the number of spectral lines for $\nu \geq 0$. We assume that these lines are located at the following wavenumber values:

$$\nu_m \triangleq \left((\ell - 1) + \frac{m-1}{N_{\text{spec}}} \right) \nu_0 \,, \;\; 1 \leq m \leq N_{\text{spec}}. \tag{1}$$

If $s_{\sigma;m}$ denotes the weight of the spectral line at $\nu = \nu_m$, then the IFGM waveform $I_\sigma(x)$ is modeled as follows:

$$I_\sigma(x) = 2\,\text{Re}\left[\sum_{m=1}^{N_{\text{spec}}} s_{\sigma;m} e^{j2\pi\nu_m x} \right] = \sum_{m=1}^{N_{\text{spec}}} \left[2\,\text{Re}[s_{\sigma;m}] \cos(2\pi\nu_m x) - 2\,\text{Im}[s_{\sigma;m}] \sin(2\pi\nu_m x) \right]. \tag{2}$$

The spectrum reconstruction problem consists of deriving the set of spectrum values $\{s_{\sigma;m}\}$ from samples of the IFGM waveform $I_\sigma(x)$. To more properly formulate this problem, we define the following vectors:

$$\mathbf{s} \triangleq \begin{bmatrix} \text{Re}[s_{\sigma;1}] \\ \vdots \\ \text{Re}\big[s_{\sigma;N_{\text{spec}}}\big] \\ \text{Im}[s_{\sigma;1}] \\ \vdots \\ \text{Im}\big[s_{\sigma;N_{\text{spec}}}\big] \end{bmatrix} \in \mathbb{R}^{2N_{\text{spec}}}, \;\; \mathbf{a}(x) \triangleq \begin{bmatrix} 2\cos(2\pi\nu_1 x) \\ \vdots \\ 2\cos\big(2\pi\nu_{N_{\text{spec}}} x\big) \\ -2\sin(2\pi\nu_1 x) \\ \vdots \\ -2\sin\big(2\pi\nu_{N_{\text{spec}}} x\big) \end{bmatrix} \in \mathbb{R}^{2N_{\text{spec}}}.$$

Then from (2), it can be seen that we have

$$I_\sigma(x) = \mathbf{a}^T(x)\,\mathbf{s}. \tag{3}$$

For the spectrum reconstruction problem, we have access to samples $I_\sigma(x_k)$ for $1 \leq k \leq N_{\text{IFGM}}$, where x_k denotes the OPD position of the k-th IFGM sample, and N_{IFGM} denotes the number of `SimCLK` IFGM samples. If we define the following quantities:

$$\mathbf{i} \triangleq \begin{bmatrix} I_\sigma(x_1) \\ \vdots \\ I_\sigma(x_{N_{\text{IFGM}}}) \end{bmatrix} \in \mathbb{R}^{N_{\text{IFGM}}}, \;\; \mathbf{A}(\mathbf{x}) \triangleq \begin{bmatrix} \mathbf{a}^T(x_1) \\ \vdots \\ \mathbf{a}^T(x_{N_{\text{IFGM}}}) \end{bmatrix} \in \mathbb{R}^{N_{\text{IFGM}} \times 2N_{\text{spec}}},$$

$$\mathbf{x} \triangleq \begin{bmatrix} x_1 \\ \vdots \\ x_{N_{\text{IFGM}}} \end{bmatrix} \in \mathbb{R}^{N_{\text{IFGM}}},$$

then from (3), we should have

$$\mathbf{i} = \mathbf{A}(\mathbf{x})\,\mathbf{s}. \tag{4}$$

Given knowledge of the `SimCLK` IFGM samples (equivalently, the vector $\mathbf{i}$), and OPD positions (equivalently, the vector $\mathbf{x}$, which implies knowledge of the matrix $\mathbf{A}(\mathbf{x})$), the

spectrum vector $\mathbf{s}$ can ostensibly be found using (4). To obtain a unique solution for $\mathbf{s}$, this requires that $N_{\text{IFGM}} \geq 2N_{\text{spec}}$.

The remainder of this article is devoted to describing the challenges that manifested with respect to solving the spectrum reconstruction problem in (4), as well as approaches considered to overcome them. These challenges consist of three main aspects: ill-conditioning of the spectrum reconstruction problem due to nonuniform sampling; imperfect knowledge of the OPD locations; and low resolution of the OPD time series mapping. Of the many methods considered to overcome these challenges, the most promising algorithms investigated here for this task are presented.

III. Ill-Conditioning of the Spectrum Reconstruction Problem with nonuniform Sampling

Nominally, TES was set up to sample the IFGM signal $I_\sigma(x)$ at integer multiples of $\lambda_0 \triangleq L\lambda_{\text{laser}}$ using the laser trigger for the IFGM ADC, which is the Nyquist rate for the signal of interest. With the `SimCLK` module in place, on average, the IFGM is sampled at integer multiples of $\widehat{\lambda}_0 \triangleq \frac{Lv}{F_{\text{IFGM,nom}}}$, where v is the average OPD scan rate of the mirror, which is ± 4.2235 cm/sec, with the sign depending upon whether or not the mirror is moving forward $(+)$ or reverse $(-)$. From the choice of operational parameters selected for TES, this implies that $\lambda_0 = L(1.06415 \times 10^{-4}$ cm) and $\widehat{\lambda}_0 = L(1.0641488 \times 10^{-4}$ cm). As such, under the case of uniform mirror velocity, the `SimCLK` module was intended to yield the same set of samples as the laser triggered sampling module, and so the `SimCLK` module would also sample the IFGM signal $I_\sigma(x)$ at the Nyquist rate.

However, as the mirror exhibits non-constant velocity, this results in a set of nonuniform samples perturbed from the Nyquist rate. This yields adjacent samples that are either too close to one another to provide enough independent information about the signal of interest, or samples that are too far apart from one another, leading to missing information. As this nonuniform sampling is a perturbation from the Nyquist rate, this suggests that with the `SimCLK` module in operation, the IFGM waveform $I_\sigma(x)$ is sub-Nyquist sampled and aliasing exists, although no formal proof of this statement is made here.

This nonuniformity of samples manifests in the ill-conditioning of the matrix $\mathbf{A}(\mathbf{x})$ from (4). An example of this is shown in Figure 3, where we have plotted the singular values of $\mathbf{A}(\mathbf{x})$ for a sample 1B2 black-body (BB) scan [6]. Here, the position vector $\mathbf{x}$ was formed by sampling the OPD time series generated by spline interpolation of the ICS time/OPD data. As can be seen, most of the singular values are approximately equal to each other, signifying that $\mathbf{A}(\mathbf{x})$ is approximately unitary, but then the singular values drop off significantly, meaning that $\mathbf{A}(\mathbf{x})$ is rank deficient. In this example, the dimension of the null space of $\mathbf{A}(\mathbf{x})$ was 100.

---

[6] Ibid.

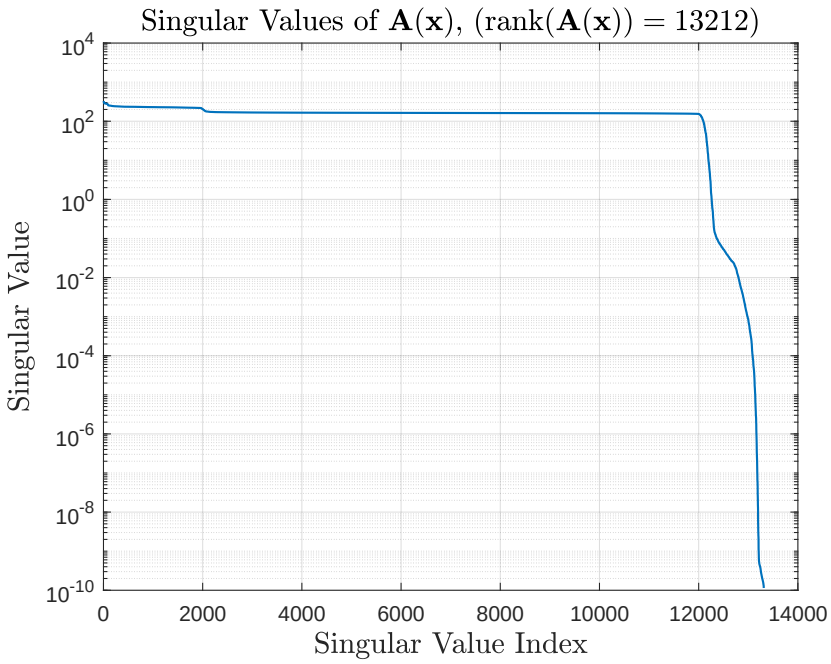

Figure 3. Singular values of the matrix $\mathbf{A}(\mathbf{x})$ for a 1B2 black-body (BB) scan. ($N_{\text{IFGM}} = 14152$, $2N_{\text{spec}} = 13312$)

The result of the ill-conditioning of the matrix $\mathbf{A}(\mathbf{x})$ is that it introduces errors in the reconstructed spectrum. From (4), the minimum norm least squares solution for the spectrum vector $\mathbf{s}$ is given by [3]

$$\widehat{\mathbf{s}} = \mathbf{A}^{\#}(\mathbf{x})\,\mathbf{i}, \tag{5}$$

where $\mathbf{A}^{\#}(\mathbf{x})$ denotes the *Moore-Penrose pseudoinverse* [3] of $\mathbf{A}(\mathbf{x})$. Using a simulated set of `SimCLK` IFGM samples, obtained from a laser-derived spectrum as shown in Figure 4(a), for reconstruction as in (5), leads to the spectrum shown in Figure 4(b). While the overall shape of the spectrum is discernible in this case, several fine details, especially for larger wavenumber ν values have been compromised.

The results shown here highlight the inherent problems with spectrum reconstruction that exist even when the sample locations $\mathbf{x}$ are known exactly. In the next section, we explore discrepancies in the OPD locations reported from the ICS. These discrepancies expose another major hurdle with respect to spectrum reconstruction: imperfect knowledge of the sample locations $\mathbf{x}$ leading to the IFGM samples $\mathbf{i}$.

IV. ICS Discrepancies in the OPD Locations

The ICS module within TES reports several location measurements, from which the OPD can be derived. Specifically, this includes the mirror encoder position (EP), the encoder digital number (EDN) (from which the EP is ostensibly derived via an affine transformation), and the laser fringe count (FC). Nominally, the EP and FC are each mapped to an OPD time series $x(t)$ as follows:

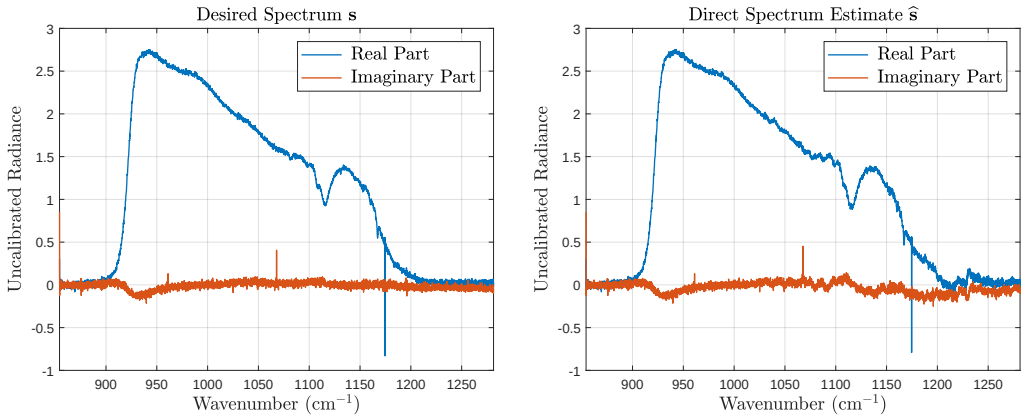

Figure 4. Spectrum reconstruction example using the minimum norm least squares solution $\widehat{\mathbf{s}}$ from (5): (a) desired spectrum obtained from 1B2 BB laser-derived samples and (b) reconstruction using simulated `SimCLK` IFGM samples derived from spline interpolation of the ICS time/OPD data.

- The EP data are multiplied by four to generate OPD data, as TES is a quadrupole interferometer [7].
- The FC data are scaled using the nominal wavelength for the Nd:YAG laser, namely $\lambda_{\text{laser}} = 1.06415 \times 10^{-4}$ cm, to generate OPD data.
- Uniform temporal sampling of the ICS at frequency $F_{\text{ICS}} = 100$ Hz is assumed.
- Interpolation is used to obtain all other (viz. non-ICS sample) OPD time series values.
- As the FC is only given in terms of a count integer, the OPD time series derived from the FC can be translated by the first EP OPD time series value in order to match the EP OPD time series at the start of each ICS data take, without loss of generality.

As mentioned earlier, as an affine transformation of the EDN can be applied to obtain the EP, the EDN can be mapped to an OPD time series using steps similar to those above. Ideally, all such OPD time series should match, however empirically, this was not found to be the case. Such discrepancies made spectrum reconstruction particularly challenging, as only the EP can be used for the cases in which the laser is not operational. This is because the EP is the only output that contains nominally reliable mirror position information in absolute units in this case.

A statistical analysis was carried out on the count sequences EDN and FC, using several ICS data captures for forward/reverse mirror scans when the TES laser was operational. The results of this analysis were later synthesized with the EP measurements to effectively compare the OPD time series resulting from each ICS output (EP, EDN, and FC).

---

[7] Ibid.

Regarding the EDN and FC count sequences, the following assumptions were made.

- The FC sequences were assumed to be the *ground truth*.
- Count values for the FC for reverse scans were negated to account for motor motion polarity.
- Each FC count sequence was translated to start at 0 for both forward/reverse scans.
- An affine transformation was applied to the EDN in order to match the FC at the beginning/ending of the observation epoch (see Sec. IV-A).

For this analysis, ICS measurements for the set of laser/`SimCLK` data captures shown in Table 1 were used. Forward and reverse scans corresponded to odd and even scan ID values, respectively. Means and standard deviations of the count sequences were generated across forward and reverse scans separately. From Table 1, it can be seen that there were 104 forward and reverse scans used for this analysis.

Table 1. List of ICS data captures used for OPD time series statistical analysis. (Uncalibrated spectrum types considered include black-body (BB), cold space (CS), and target (TGT)) [8].

Laser			SimCLK		
Run ID	Spectrum Type ID	Scan IDs	Run ID	Spectrum Type ID	Scan IDs
27717	BB	00-19	27710	BB	00-19
27727	CS	00-09	27711	CS	00-09
27728	TGT	00-43	27712	TGT	00-43
27729	CS	00-09	27713	CS	00-09
27745	BB	00-19	27765	BB	00-19

A. Affine Transformation of EDN to Match FC Boundaries

As mentioned above, for the statistical analysis of the EDN and FC count sequences, an affine transformation was applied to the EDN to match the ground truth FC at the beginning/ending of each observation epoch. This was done in order to adhere to the logical assumption that regardless of the paths taken by the EDN and FC, both should start and finish at the same effective mirror location.

Quantitatively, suppose that the number of ICS data points for a given scan is N_{ICS}. If $\{c_{\text{EDN}}[n]\}_{n=0}^{N_{\text{ICS}}-1}$ and $\{c_{\text{FC}}[n]\}_{n=0}^{N_{\text{ICS}}-1}$ denote the EDN/FC ICS count outputs, respectively, then we seek an affine transformation of the form:

$$\widetilde{c}_{\text{EDN}}[n] = mc_{\text{EDN}}[n] + b\,,\ 0 \leq n \leq N_{\text{ICS}} - 1, \tag{6}$$

where the slope m and intercept b are chosen such that

$$\widetilde{c}_{\text{EDN}}[0] = c_{\text{FC}}[0]\ ,\ \widetilde{c}_{\text{EDN}}[N_{\text{ICS}} - 1] = c_{\text{FC}}[N_{\text{ICS}} - 1]\,.$$

[8] Ibid.

Elementary linear algebra shows m and b can be found by solving the following linear system:

$$\begin{bmatrix} m \\ b \end{bmatrix} = \begin{bmatrix} c_{\mathrm{EDN}}[0] & 1 \\ c_{\mathrm{EDN}}[N_{\mathrm{ICS}}-1] & 1 \end{bmatrix}^{-1} \begin{bmatrix} c_{\mathrm{FC}}[0] \\ c_{\mathrm{FC}}[N_{\mathrm{ICS}}-1] \end{bmatrix}.$$

Note that the slope m is dimensionless, whereas the intercept b has the "units" of counts. A statistical analysis was carried out on the dimensionless discrete-time sequences $c_{\mathrm{FC}}[n]$ and $\widetilde{c}_{\mathrm{EDN}}[n]$ (as well as other sequences derived from them). Mapping to the EP (and equivalently the OPD) was only carried out at the end to infer the conversion factor from EDN to EP.

B. Nominal Count Sequences

A plot of the mean value (plus/minus one standard deviation) of the nominal count sequences $c_{\mathrm{FC}}[n]$ and $\widetilde{c}_{\mathrm{EDN}}[n]$ is shown Figure 5(a) for forward scans and Figure 5(b) for reverse scans. As mentioned earlier, each FC sequence was translated to start at 0 for both forward/reverse scans (i.e., the condition $c_{\mathrm{FC}}[0] = 0$ was enforced). From these plots, it can be seen that the FC and the transformed EDN appear to match very well. However, the dominant linear trend to the data obscures the differences between these sequences.

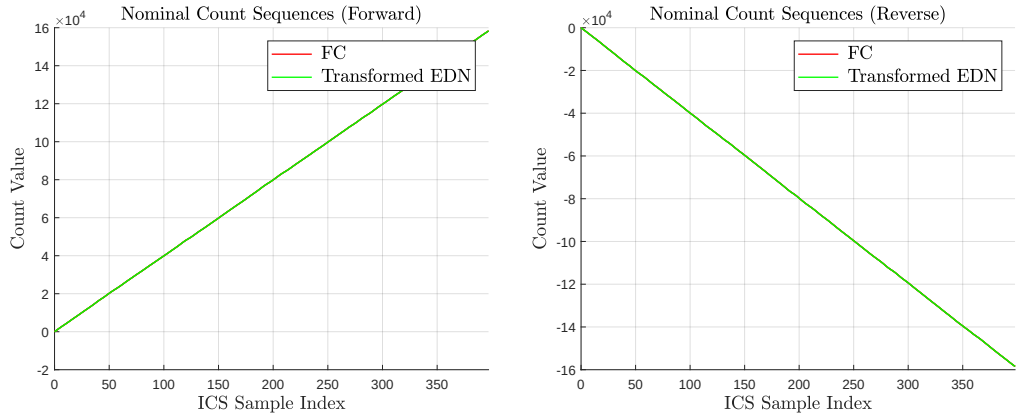

(a) (b)

Figure 5. Mean plus/minus one standard deviation of the nominal count sequences $c_{\mathrm{FC}}[n]$ and $\widetilde{c}_{\mathrm{EDN}}[n]$: (a) forward scans and (b) reverse scans.

C. Residual Count Sequences

The ensemble mean values (plus/minus one standard deviation) of the residual count sequences (in which a least squares affine trend was removed from each) are shown in Figure 6. From this, it can be seen that the forward and reverse scans appear relatively consistent and repeatable, respectively. However, it can be seen that deviations exist between the FC and the transformed EDN count sequences.

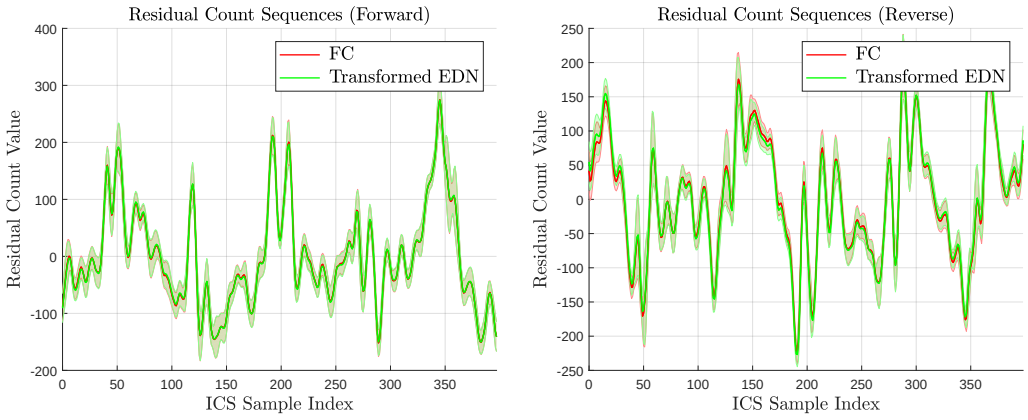

Figure 6. Mean plus/minus one standard deviation of the FC and the transformed EDN residual count sequences: (a) forward scans and (b) reverse scans.

D. Backward Difference Sequences

A statistical analysis was also carried out for the backward difference sequences given below:

$$\Delta_{\mathrm{FC}}[n] \triangleq c_{\mathrm{FC}}[n] - c_{\mathrm{FC}}[n-1]\,, \tag{7}$$

$$\widetilde{\Delta}_{\mathrm{EDN}}[n] \triangleq \widetilde{c}_{\mathrm{EDN}}[n] - \widetilde{c}_{\mathrm{EDN}}[n-1]\,, \tag{8}$$

with the initialization $c_{\mathrm{FC}}[-1] = 0$ and $\widetilde{c}_{\mathrm{EDN}}[-1] = 0$. These difference sequences represent an approximation to the velocity of the mirror location as a function of time. Specifically, if the count sequences are mapped to OPD location values, then the backward difference of these sequences multiplied by the sample rate F_{ICS} will approximately correspond to the velocity of the mirror location at the sample time under consideration.

Plots of the mean values (plus/minus one standard deviation) of the backward difference sequences can be found in Figure 7 for the forward (a) and reverse (b) scan directions. From these plots, it can be seen that, as before, the forward and reverse scans appear relatively repeatable and consistent, respectively. An interesting observation that can be made is that for both forward/reverse cases, the count differences span a range of more than 120 counts/sample.

E. FC/Transformed EDN Count Difference Sequence

To highlight the discrepancies between the FC and the transformed EDN count sequences, a statistical analysis was carried out for the raw difference between the two sequences, defined as follows:

$$d[n] \triangleq c_{\mathrm{FC}}[n] - \widetilde{c}_{\mathrm{EDN}}[n]\,. \tag{9}$$

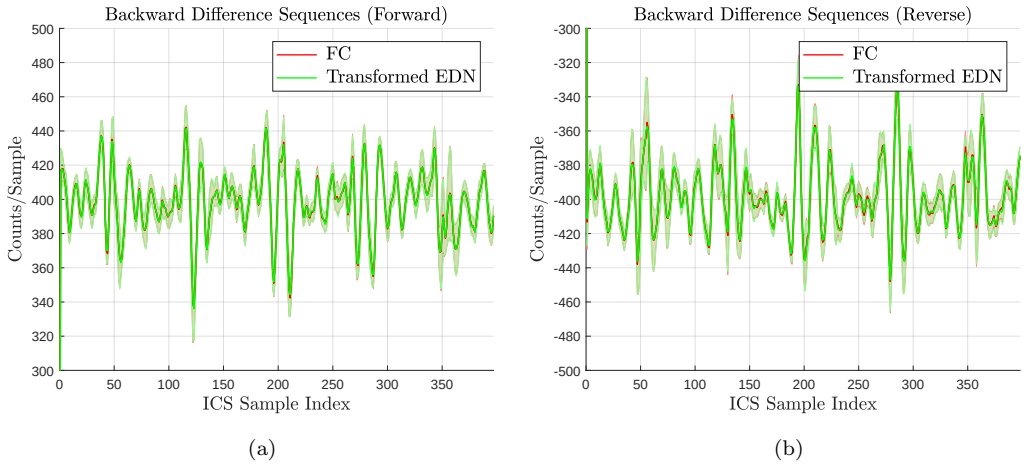

Figure 7. Mean plus/minus one standard deviation of the backward difference sequences $\Delta_{\mathrm{FC}}[n]$ and $\widetilde{\Delta}_{\mathrm{EDN}}[n]$ from (7) and (8), respectively: (a) forward scans and (b) reverse scans.

Plots of the mean (plus/minus one standard deviation) of the difference signal $d[n]$ from (9) are shown in Figure 8. From these plots, it can be seen that a nonlinear drift component exists between the FC and the transformed EDN count sequences. Furthermore, on average, the count discrepancy can be less than -5 counts for forward scans and greater than 15 counts for reverse scans. In addition, the deviation of the count discrepancies from the mean value is on the order of ± 5 counts for both forward/reverse scans. (As expected, the mean and standard deviation is zero at the beginning/ending of the observation epoch due to boundary matching.)

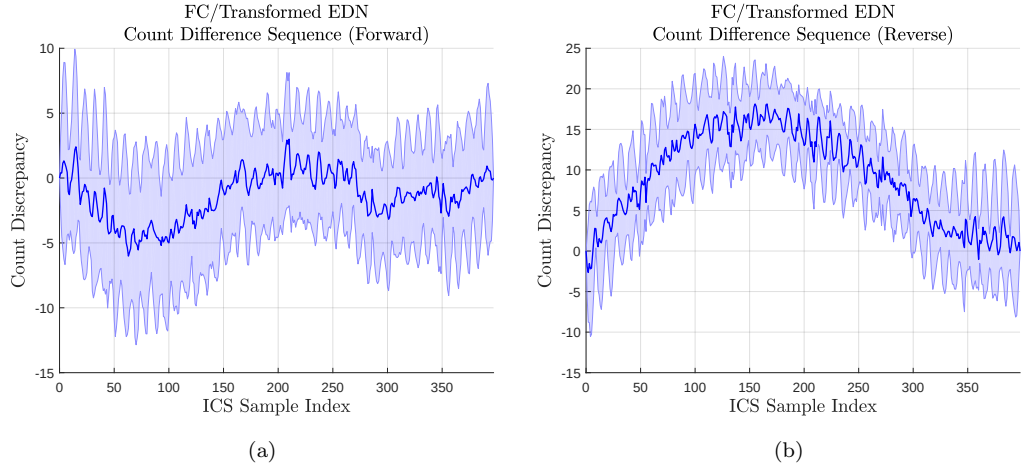

Figure 8. Mean plus/minus one standard deviation of the FC/transformed EDN count difference sequence $d[n]$ from (9): (a) forward scans and (b) reverse scans.

In Figure 9, plots of the mean (plus/minus one standard deviation) of the detrended count difference sequences are given. From these plots, as well as those from Figure 8, it can be seen that the detrended difference between the FC and the transformed EDN counts exhibits two primary components: a high amplitude/low frequency

non-stationary wander component, and a low amplitude/high frequency periodic component. Furthermore, the residual periodic component is more noticeable in the reverse scans than the forward ones.

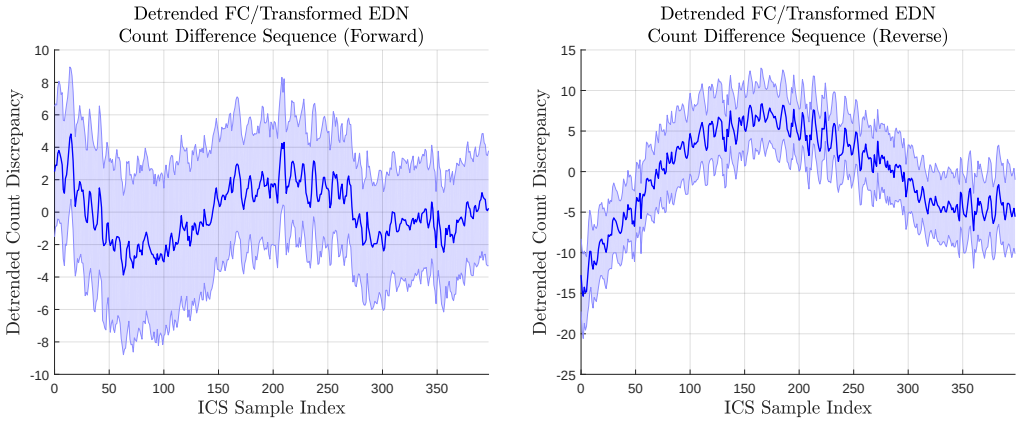

Figure 9. Mean plus/minus one standard deviation of the detrended FC/transformed EDN count difference sequence: (a) forward scans and (b) reverse scans.

F. Difference of FC/Transformed EDN Backward Difference Sequences

As a final sequence upon which to statistically characterize the ICS outputs, the difference of the FC/transformed EDN backward difference sequences was considered. Specifically, a statistical analysis of the following sequence was carried out:

$$D[n] \triangleq \Delta_{\mathrm{FC}}[n] - \widetilde{\Delta}_{\mathrm{EDN}}[n]\,, \tag{10}$$

where $\Delta_{\mathrm{FC}}[n]$ and $\widetilde{\Delta}_{\mathrm{EDN}}[n]$ are as in (7) and (8), respectively.

Plots of the mean (plus/minus one standard deviation) of the difference of backward difference sequences $D[n]$ from (10) are shown in Figure 10. From these plots, it can be seen that, on average, the difference between the counts per sample for the FC and the transformed EDN is approximately zero, but that it can deviate on the order of ± 4 counts/sample.

While the results from Figure 10 may not appear overly pertinent, interesting observations can be made from the *autocorrelation* sequence [2] derived from $D[n]$. For the case of finite-length data, the autocorrelation sequence $\widehat{R}_D[k]$ is calculated as follows in this setting:

$$\widehat{R}_D[k] \triangleq \begin{cases} \dfrac{1}{N_{\mathrm{ICS}} - k} \displaystyle\sum_{n=k}^{N_{\mathrm{ICS}}-1} D[n]\, D^*[n-k]\,, & 0 \le k \le N_{\mathrm{ICS}} - 1, \\ 0, & k \ge N_{\mathrm{ICS}}, \\ \widehat{R}_D^*[-k]\,, & k \le -1. \end{cases} \tag{11}$$

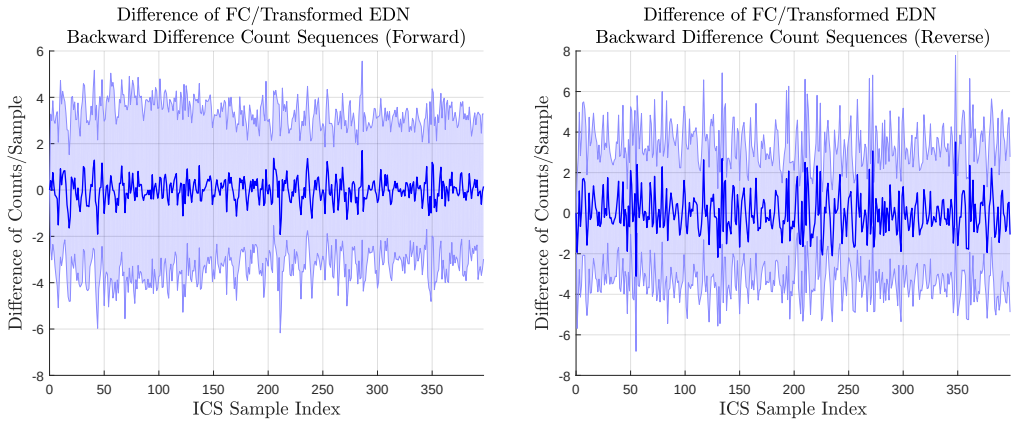

(a) (b)

Figure 10. Mean plus/minus one standard deviation of the difference of FC/transformed EDN backward difference sequences $D[n]$ from (10): (a) forward scans and (b) reverse scans.

Here k represents the *lag* between sequence overlaps [2]. The function $\widehat{R}_D[k]$ from above is an *unbiased* estimate of the true autocorrelation $R_D[k] \triangleq E\left[D[n]\, D^*[n-k]\right]$ (assuming $D[n]$ if is a *wide sense stationary* (WSS) process) [2].

Plots of the mean (plus/minus one standard deviation) of the autocorrelation sequence $\widehat{R}_D[k]$ from (11) are shown in Figure 11. From these plots, it can be seen that a very noticeable periodic component exists and appears to be at the same frequency for both the forward and reverse scans.

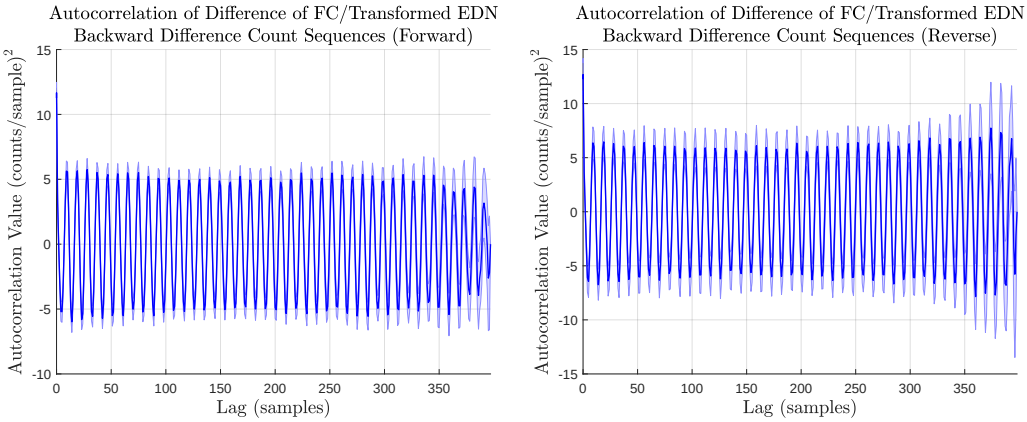

(a) (b)

Figure 11. Mean plus/minus one standard deviation of the autocorrelation sequence $\widehat{R}_D[k]$ from (11): (a) forward scans and (b) reverse scans.

To cull the periodic content of the autocorrelation sequence observed in Figure 11, a suitable way is to calculate the *power spectral density* (PSD) [2]. This is computed as follows:

$$\widehat{S}_D(f) \triangleq \sum_{k\in\mathbb{Z}} \widehat{R}_D[k]\, e^{-j2\pi fk}, \tag{12}$$

where f is the *normalized frequency* given by $f = \frac{F}{F_s}$, with F begin the analog frequency of the underlying time series and F_s being the sample rate of the discrete-time sequence (nominally F_{ICS} here) [2]. The PSD is always non-negative (i.e., $\widehat{S}_D(f)$ for all f) and is even here (i.e., $\widehat{S}_D(f) = \widehat{S}_D(-f)$ for all f), as $\widehat{R}_D[k]$ is real in this setting [2].

Plots of the mean (plus/minus one standard deviation) of the PSD $\widehat{S}_D(f)$ from (12), calculated in decibel (dB) units, are shown in Figure 12. From these plots, a dominant spectral component at $f = 0.10742$ can be seen for both the forward and reverse scans. Assuming the sampling frequency is $F_{\text{ICS}} = 100$ Hz, then the dominant spectral component occurs at a frequency of 10.742 Hz for both forward/reverse scans.

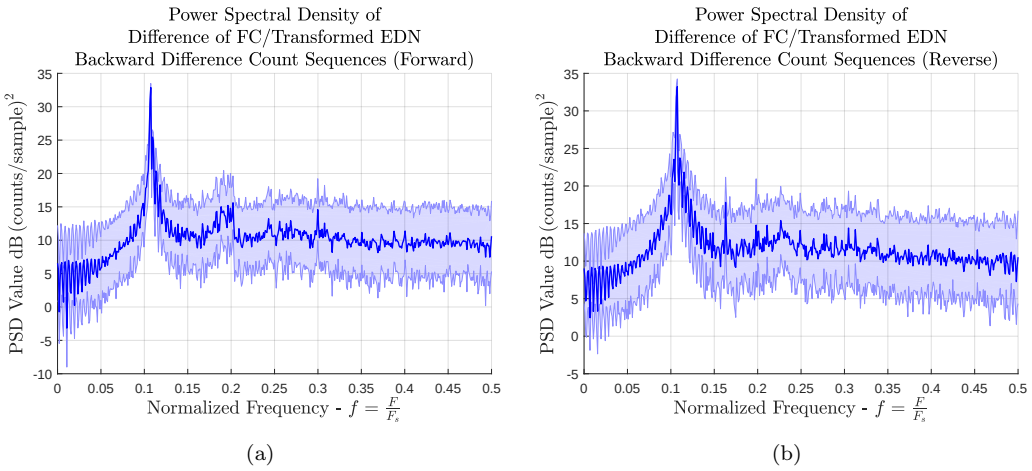

Figure 12. Mean plus/minus one standard deviation of the power spectral density (PSD) $\widehat{S}_D(f)$ from (12) in dB units: (a) forward scans and (b) reverse scans.

G. Empirical Distribution of EDN Affine Transformation Parameters

Histogram and kernel density estimate (KDE) plots of the affine transformation parameters of the slope m and intercept b from (6) were generated. Specifically, the histogram and KDE plots for the slope m are given in Figure 13, while those for the intercept b are given in Figure 14. From the analysis carried out here, the following was ascertained:

- Mean of slope m: 3.4387 (forward), 3.4386 (reverse).
- Standard deviation of slope m: 1.5854×10^{-4} (forward), 2.0194×10^{-4} (reverse).
- Mean of intercept b: -412003.7856 counts (forward), -570499.4462 counts (reverse).
- Standard deviation of intercept b: 140.3222 counts (forward), 130.7771 counts (reverse).

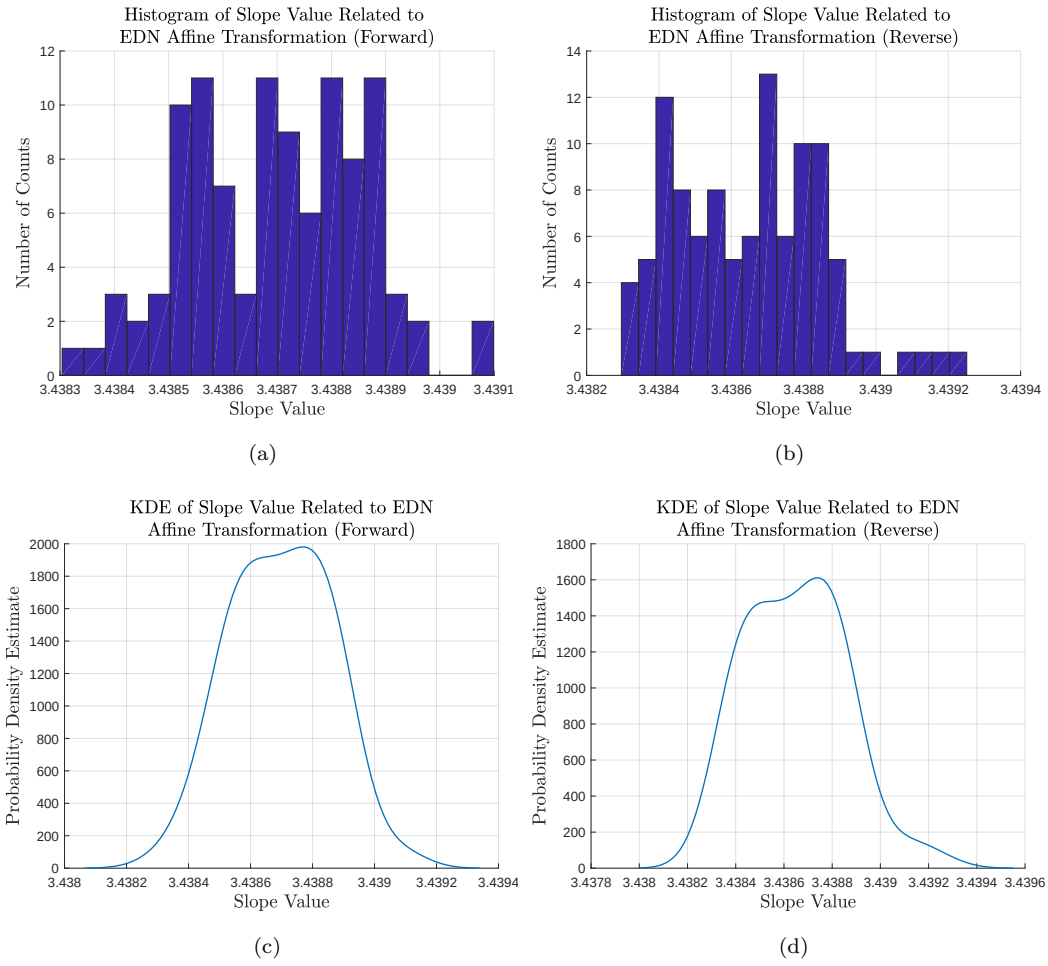

Figure 13. Histogram and kernel density estimate (KDE) plots for the slope parameter m from (6): (a) histogram for the forward scans, (b) histogram for the reverse scans, (c) KDE for the forward scans, (d) KDE for the reverse scans.

From the KDE plots in Figure 13, it can be seen that for the slope m, the distribution for the forward scans is weakly bimodal and appears approximately normal, whereas for the reverse scans, the distribution has a more pronounced bimodality and exhibits a noticeable skew from normality. Regarding the intercept b, from the KDE plots in Figure 14, the distribution for the forward scans appears clearly bimodal with peaks at approximately -4.121×10^5 counts and -4.118×10^5 counts, while for the reverse scans, the distribution seems approximately unimodal, but with significant negative skew.

H. Mapping Count Values to OPD and EP

Recall from the beginning of Sec. IV that from the FC nominal count sequence $c_{\mathrm{FC}}[n]$, the sequence of FC-derived OPD values $x_{\mathrm{FC}}[n]$ is given as follows:

$$x_{\mathrm{FC}}[n] = \lambda_L c_{\mathrm{FC}}[n]\,.$$

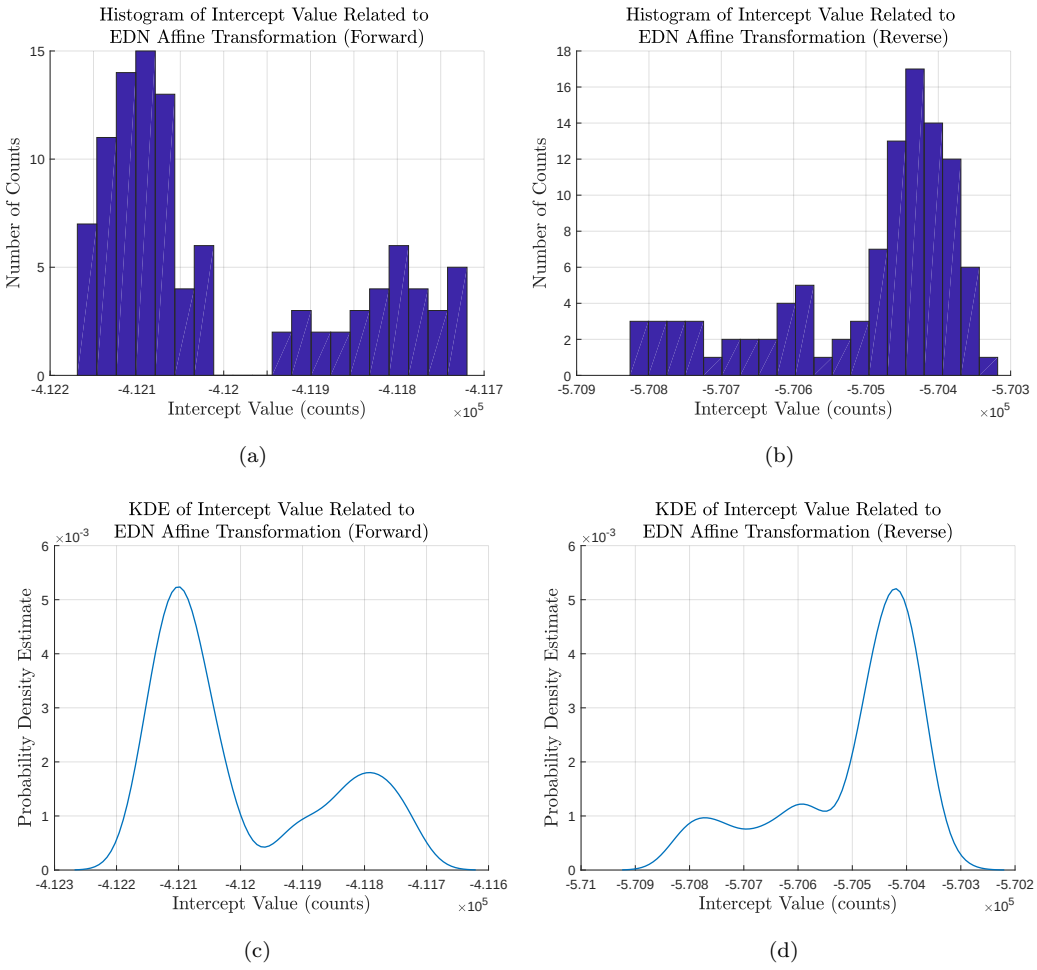

Figure 14. Histogram and kernel density estimate (KDE) plots for the intercept parameter b from (6): (a) histogram for the forward scans, (b) histogram for the reverse scans, (c) KDE for the forward scans, (d) KDE for the reverse scans.

Assuming the transformed EDN count sequence $\widetilde{c}_{\mathrm{EDN}}[n]$ satisfies $\widetilde{c}_{\mathrm{EDN}}[n] \approx c_{\mathrm{FC}}[n]$, then the sequence of OPD values derived from this, denoted here by $x_{\mathrm{EDN}}[n]$, is given by:

$$x_{\mathrm{EDN}}[n] \triangleq \lambda_L \widetilde{c}_{\mathrm{EDN}}[n] = (\lambda_L m)\, c_{\mathrm{EDN}}[n] + (\lambda_L b)\,,$$

where the last equation follows from (6). From this, it can be seen that the ICS EDN values can be converted to OPD via the following slope/intercept affine transformation:

$$\begin{aligned} \text{slope, scale factor: } K_{\mathrm{EDN}\to\mathrm{OPD}} &\triangleq \lambda_L m\,, \\ \text{intercept, offset: } O_{\mathrm{EDN}\to\mathrm{OPD}} &\triangleq \lambda_L b\,. \end{aligned}$$

As TES is a quadrupole-type interferometer [9], the EP is four times smaller than the OPD, meaning that the conversion from EDN to EP is described as follows:

$$\begin{aligned} \text{slope, scale factor: } K_{\text{EDN}\to\text{EP}} &\triangleq (\lambda_L m)/4\,, \\ \text{intercept, offset: } O_{\text{EDN}\to\text{EP}} &\triangleq (\lambda_L b)/4\,. \end{aligned}$$

Using the mean values obtained from the statistical analysis performed, we have

$$\begin{aligned} K_{\text{EDN}\to\text{EP}} &= 9.14823\times10^{-5}\text{ cm} \quad \text{(forward)}\,, \quad 9.14809\times10^{-5}\text{ cm} \quad \text{(reverse)}\,, \\ O_{\text{EDN}\to\text{EP}} &= -10.96085\text{ cm} \quad\quad\;\; \text{(forward)}\,, \quad -15.17742\text{ cm} \quad\quad\;\; \text{(reverse)}\,. \end{aligned}$$

These values can be compared with those obtained using the actual EP data from the ICS. In Figure 15(a), we have plotted the raw ICS EP values observed as a function of the EDN values observed for the forward scans, along with the residuals from a linear regression (least squares affine transformation fit) in Figure 15(b). Similarly, we have plotted these quantities for the reverse scans in Figure 16. From these figures, it can be seen that the mapping between EP and EDN is well approximated using an affine transformation, with the error appearing to be approximately due to quantization error (as the residuals appear to be uniformly distributed).

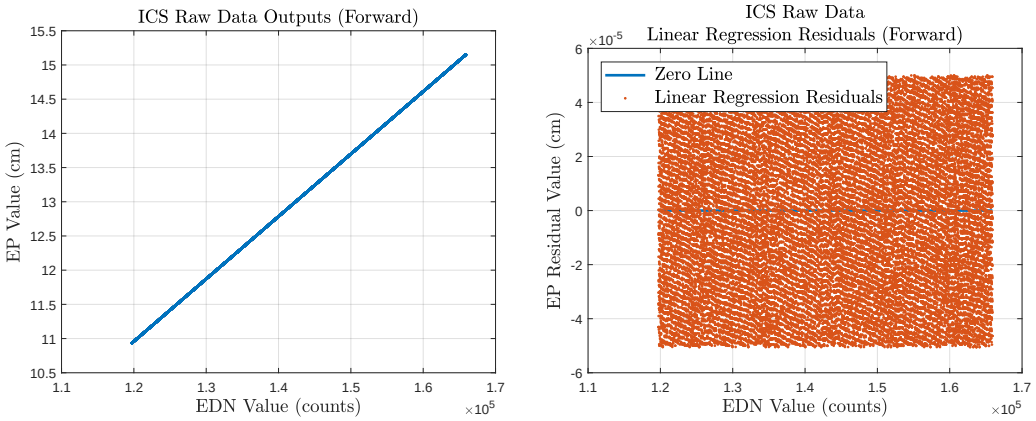

(a) (b)

Figure 15. Analysis of ICS raw data outputs for the forward scans: (a) scatter plot of observed EP values as a function of observed EDN values, (b) residuals from a linear regression of the EP as a function of the EDN.

From the results of the EP/EDN linear regression analysis, the following was found:

$$\begin{aligned} \text{slope, scale factor:} \quad \widehat{K}_{\text{EDN}\to\text{EP}} &= 9.13242\times10^{-5}\text{ cm} \quad \text{(forward)}\,, \\ \text{intercept, offset:} \quad \widehat{O}_{\text{EDN}\to\text{EP}} &= 5.03462\times10^{-7}\text{ cm} \quad \text{(forward)}\,, \\ \text{slope, scale factor:} \quad \widehat{K}_{\text{EDN}\to\text{EP}} &= 9.13242\times10^{-5}\text{ cm} \quad \text{(reverse)}\,, \\ \text{intercept, offset:} \quad \widehat{O}_{\text{EDN}\to\text{EP}} &= 2.44339\times10^{-6}\text{ cm} \quad \text{(reverse)}\,. \end{aligned}$$

The slope scale factors obtained here using linear regression can be compared with those obtained by relating the EDN to the EP using the FC-derived OPD as the

[9] Ibid.

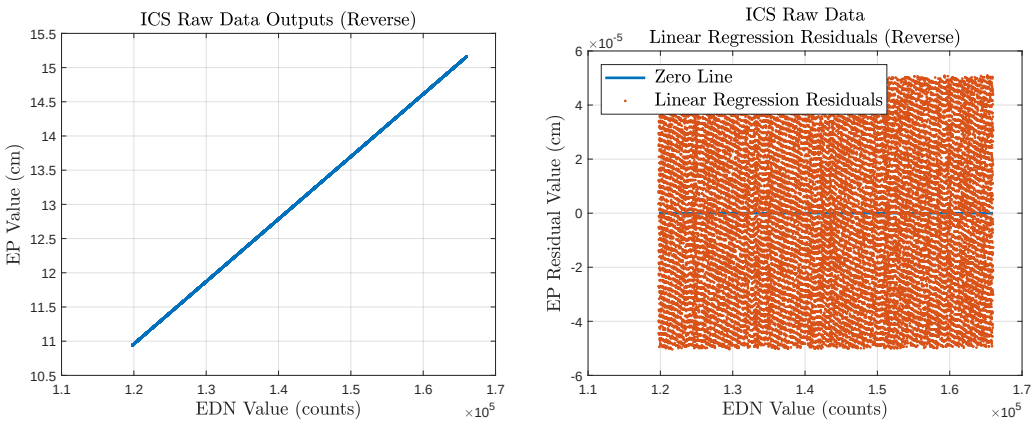

(a) (b)

Figure 16. Analysis of ICS raw data outputs for the reverse scans: (a) scatter plot of observed EP values as a function of observed EDN values, (b) residuals from a linear regression of the EP as a function of the EDN.

ground truth. In particular, compare the following forward/reverse conversion scale factors:

$$\begin{aligned} \text{forward:} \quad & K_{\text{EDN}\to\text{EP}} = 9.14823\times10^{-5}\ \text{cm}, \quad \widehat{K}_{\text{EDN}\to\text{EP}} = 9.13242\times10^{-5}\ \text{cm}, \\ \text{reverse:} \quad & K_{\text{EDN}\to\text{EP}} = 9.14809\times10^{-5}\ \text{cm}, \quad \widehat{K}_{\text{EDN}\to\text{EP}} = 9.13242\times10^{-5}\ \text{cm}. \end{aligned}$$

As can be seen, the conversion factors are within about 0.17% of one another for both the forward and reverse scan cases.

I. Summary of ICS Data Output Analysis

Combining the results of the analysis provided Sec. IV-E and IV-H, it follows that the discrepancy between the OPD time series derived from the EP and FC can be on the order of 10^{-3} cm. In other words, assuming the FC represents the ground truth with respect to the OPD (which is approximately valid when the TES laser is operational), the EP output can be off from the true OPD location on the order of 10^{-3} cm. This made the problem of reconstructing spectra using `SimCLK` samples very challenging for the case in which the TES laser was not operational, as only the EP could be relied upon to provide any nominally accurate OPD location information.

V. Low Resolution of ICS OPD Measurements

In addition to there being a discrepancy between ICS OPD position measurements, the rate at which ICS OPD locations are reported is significantly sub-sampled with respect to the `SimCLK` IFGM sample rate. For example, from Figure 1, the ICS reports OPD location information at a rate of $F_{\text{ICS}} = 100$ Hz, while for a 1B2 scan, for which

the divisor factor $L = 11$ [10], the SimCLK IFGM sample rate is approximately $F_{\mathrm{IFGM}} = 3.6$ kHz.

To see why this can be problematic, note that in order to map the SimCLK sample times to OPD locations, we need access to the true OPD time series $x(t)$. Specifically, if $\{t_k\}_{k=1}^{N_{\mathrm{IFGM}}}$ denotes the set of SimCLK IFGM sample times, then this set must be mapped to the set of OPD locations $\{x_k\}_{k=1}^{N_{\mathrm{IFGM}}}$ using the relation $x_k = x(t_k)$ for all k, in order to form the vector $\mathbf{x}$ appearing in (4).

In practice, the ICS will output a set of time/OPD position tuples of the form $(t, x) \in \left\{\left(\frac{n-1}{F_{\mathrm{ICS}}}, \widetilde{x}_n\right)\right\}_{n=1}^{N_{\mathrm{ICS}}}$, where N_{ICS} is the number of ICS data capture samples for a given scan, and $\widetilde{x}_n$ denotes the n-th OPD position value (which could be from the EP or FC outputs, but in truth may be something entirely different). From these knot values $\left\{\left(\frac{n-1}{F_{\mathrm{ICS}}}, \widetilde{x}_n\right)\right\}_{n=1}^{N_{\mathrm{ICS}}}$, the OPD time series is constructed via interpolation, using either a sinc, spline, or piecewise cubic Hermite interpolating polynomial (PCHIP) type interpolant.

While a spectral analysis of the ICS OPD sample values carried out previously suggested that the mirror movement should be sufficiently smooth to be reasonably characterized by samples obtained at a rate of $F_{\mathrm{ICS}} = 100$ Hz, minute high frequency information on the mirror movement may have been lost by sampling at this low rate. Loss of this high frequency information could be especially deleterious in light of the fact that the IFGM waveforms are all *bandpass* sampled here.

As an example, consider the laser-derived 1B2 BB IFGM waveform shown in Figure 17, where we have phase aligned the ZPD to occur at $x = 0$ and have zoomed in to the region near the ZPD, where 99.9% of the IFGM energy is contained. In addition to plotting the IFGM waveform, we have also plotted the SimCLK samples as well as the samples corresponding to the ICS EP OPD locations for this scan. Here, the SimCLK OPD locations were obtained by PCHIP interpolation of the ICS EP OPD knot values.

From Figure 17, several important observations can be made. First, the samples corresponding to the ICS EP OPD locations are spaced apart far enough away as to entirely miss the ZPD portion of the IFGM waveform. From this, it is clear that several of the most critical SimCLK IFGM samples rely heavily upon the fidelity of the OPD time series representation in between the knot values $\left\{\left(\frac{n-1}{F_{\mathrm{ICS}}}, \widetilde{x}_n\right)\right\}_{n=1}^{N_{\mathrm{ICS}}}$. In this case, there are approximately 35 SimCLK samples contained between adjacent ICS EP OPD values. Thus, in addition to the discrepancy of OPD locations reported from the ICS, such as that between the EP and FC outputs, the vast majority of SimCLK IFGM samples must be derived by interpolation of the ICS OPD knot values, which may or may not correspond to the actual OPD time series $x(t)$.

---

[10] Ibid.

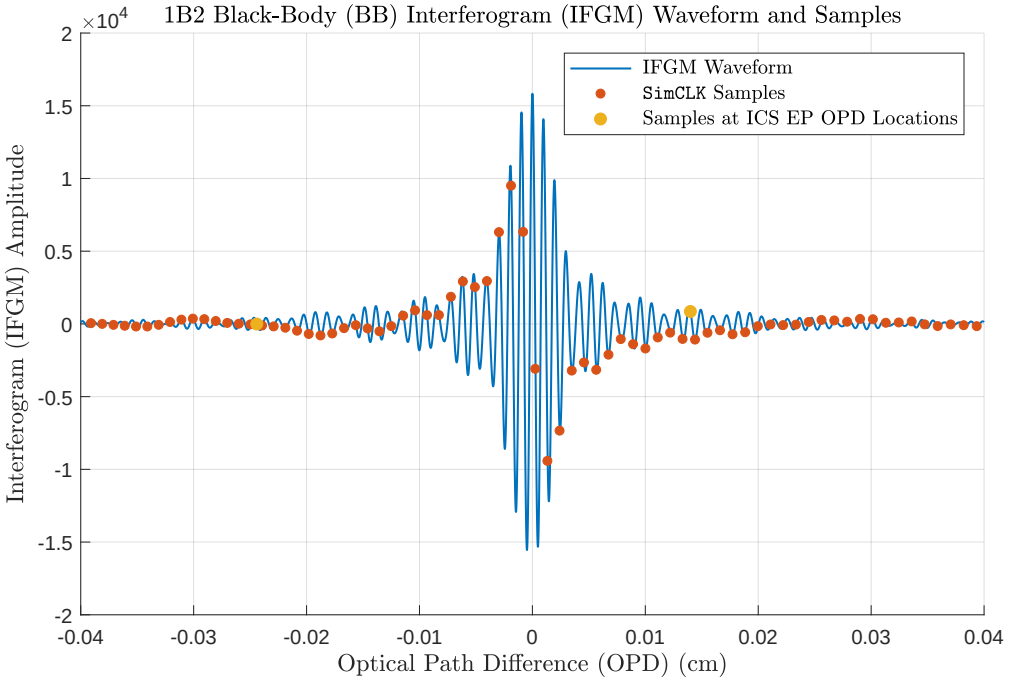

Figure 17. Plot of 1B2 black-body (BB) IFGM wavform along with `SimCLK` samples and samples corresponding to the ICS EP OPD locations. (Data taken from laser data capture - run ID: 27717, scan ID: 01, pixel ID: 07.)

Another issue that is apparent from Figure 17 is the sensitivity of the `SimCLK` samples to OPD location errors. This is due to the fact that the IFGM waveforms are bandpass signals. For example, the `SimCLK` IFGM sample closest to the ZPD corresponds to the OPD location $x = 2.8 \times 10^{-4}$ cm with an amplitude value of -3108. A slight perturbation of this sample to the ZPD at $x = 0$ would lead to an amplitude value of 15825, which would dramatically affect spectrum reconstruction performance if such position errors are not known and accommodated.

Heuristically, the sensitivity of the spectrum reconstruction problem to OPD locations errors can be characterized by the center bandpass frequency of the IFGM waveform. Referring to Figure 2, the center bandpass frequency ν_c is defined as follows:

$$\nu_c \triangleq \left(\ell - \frac{1}{2}\right)\nu_0.$$

The reciprocal of this quantity, $X_c \triangleq \frac{1}{\nu_c}$, which will be referred to here as the center bandpass period, is an approximate measure of the period between local variations of the IFGM waveform. For example, for 1B2, we have $\ell = 3$ and $\nu_0 = 427.144$ cm^{-1} [11], from which we have

$$\nu_c = 1067.86 \text{ cm}^{-1}, \; X_c = 9.36452 \times 10^{-4} \text{ cm}. \tag{13}$$

[11] Ibid.

Careful inspection of the IFGM waveform plotted in Figure 17 shows that the distance between local peaks/troughs is about 9.717×10^{-4} cm, a number which is very close to the center bandpass period X_c.

A final point which should be made with respect to mapping `SimCLK` sample times to OPD position locations regards the timing offset issue. The `SimCLK` IFGM and ICS data files each contain a *Temps atomique international* (TAI) timestamp which nominally corresponds to the first data sample, respectively. Alignment of these timestamps is crucial for selecting the proper `SimCLK` sample times to feed into the OPD time series for subsequent reconstruction. Unfortunately, the uncertainty of these TAI timestamps with respect to the first data sample is not known exactly and may be as large as a single ICS data sample step interval (i.e., 0.01 sec).

Given the inherent discrepancy between ICS OPD location outputs, coupled with the low resolution of the OPD time series knot values supplied by the ICS, and the unknown timing offset between the `SimCLK` IFGM and ICS data capture files, we opted to consider spectrum reconstruction algorithms for which the OPD sample locations were either unknown or imperfect.

VI. Tikhonov Regularized Spectrum Reconstruction with Unknown/Imperfect Sample Locations

To overcome the ill-conditioning of the nominal spectrum reconstruction problem, we considered adding a Tikhonov regularization term, which can incorporate a priori knowledge of the spectrum to be reconstructed. Specifically, we focused on optimizing the following objective, which is a function of both the OPD sample position vector $\mathbf{x}$ and the spectrum vector $\mathbf{s}$:

$$\xi(\mathbf{x}, \mathbf{s}) \triangleq ||\mathbf{A}(\mathbf{x})\,\mathbf{s} - \mathbf{i}||^2_{\mathbf{P}} + ||\mathbf{s} - \mathbf{s}_0||^2_{\mathbf{Q}}\,. \tag{14}$$

Here, $||\mathbf{y}||^2_{\mathbf{R}} \triangleq \mathbf{y}^\dagger \mathbf{R}\mathbf{y}$ for $\mathbf{R} \succeq \mathbf{0}$ is the squared norm of $\mathbf{y}$ weighted by $\mathbf{R}$, and we have

- $\mathbf{P}$: $N_{\text{IFGM}} \times N_{\text{IFGM}}$ mean squared error (MSE) weighting matrix which satisfies $\mathbf{P} \succeq \mathbf{0}$,
- $\mathbf{Q}$: $2N_{\text{spec}} \times 2N_{\text{spec}}$ a priori (AP) spectral error weighting matrix which satisfies $\mathbf{Q} \succeq \mathbf{0}$,
- $\mathbf{s_0}$: $2N_{\text{spec}} \times 1$ AP spectrum error vector target value.

The Tikhonov regularization problem (TRP) in (14) has a Bayesian interpretation, in which $\mathbf{P}$ and $\mathbf{Q}$ represent the inverse covariance matrices of $\mathbf{i}$ and $\mathbf{s}$, respectively, and $\mathbf{s_0}$ represents the mean or expected value of $\mathbf{s}$.

The *globally* optimal value of the spectrum $\mathbf{s}$ for a fixed OPD position vector $\mathbf{x}$ is given by the following [3].

$$\mathbf{s}_{\text{opt}}(\mathbf{x}) = \left(\mathbf{A}^\dagger(\mathbf{x})\,\mathbf{P}\mathbf{A}(\mathbf{x}) + \mathbf{Q}\right)^{-1} \left(\mathbf{A}^\dagger(\mathbf{x})\,\mathbf{P}\mathbf{i} + \mathbf{Q}\mathbf{s}_0\right). \tag{15}$$

Substituting $\mathbf{s}_{\text{opt}}(\mathbf{x})$ in (14) leads to a new objective that is only a function of $\mathbf{x}$:

$$\zeta(\mathbf{x}) \triangleq \xi(\mathbf{x}, \mathbf{s}_{\text{opt}}(\mathbf{x})) = \mathbf{i}^{\dagger}\mathbf{P}\left(\mathbf{i} - \mathbf{A}(\mathbf{x})\,\mathbf{s}_{\text{opt}}(\mathbf{x})\right) + \mathbf{s}_0^{\dagger}\mathbf{Q}\left(\mathbf{s}_0 - \mathbf{s}_{\text{opt}}(\mathbf{x})\right). \tag{16}$$

The expression for the new TRP objective $\zeta(\mathbf{x})$ from above can be interpreted as the sum of two weighted cross-correlation terms: one between the IFGM samples and the reconstruction error, and the other between the AP spectrum and the spectrum deviation from the AP value.

A. Gradient of the Spectrum-Optimized TRP Objective

A gradient descent algorithm was developed to minimize the spectrum-optimal TRP objective from (16). To calculate the desired gradient $\nabla\zeta(\mathbf{x})$, the differential of $\zeta(\mathbf{x})$, namely $d(\zeta(\mathbf{x}))$, was first computed. From the differential $d(\zeta(\mathbf{x}))$, the gradient vector $\nabla\zeta(\mathbf{x})$ can be obtained by using the expression

$$d(\zeta(\mathbf{x})) = (d\mathbf{x})^{T}\,\nabla\zeta(\mathbf{x}), \tag{17}$$

and extracting the coefficients of dx_k for $1 \le k \le N_{\text{IFGM}}$.

Calculation of $d(\zeta(\mathbf{x}))$ was facilitated by exploiting the fact that for an invertible matrix $\mathbf{Z} \in \mathbb{C}^{m\times m}$, we have

$$d\big(\mathbf{Z}^{-1}\big) = -\mathbf{Z}^{-1}\,(d\mathbf{Z})\,\mathbf{Z}^{-1}.$$

Using this result, if we define

$$\boldsymbol{\epsilon}_{\text{opt}}(\mathbf{x}) \triangleq \mathbf{A}(\mathbf{x})\,\mathbf{s}_{\text{opt}}(\mathbf{x}) - \mathbf{i}, \tag{18}$$

to be the error vector obtained from the spectrum vector $\mathbf{s}_{\text{opt}}(\mathbf{x})$ from (15), then, after some algebraic manipulation, it can be shown that we have

$$d(\zeta(\mathbf{x})) = \left((d(\mathbf{A}(\mathbf{x})))\,\mathbf{s}_{\text{opt}}(\mathbf{x})\right)^{\dagger}\left(\mathbf{P}\boldsymbol{\epsilon}_{\text{opt}}(\mathbf{x})\right) + \left(\mathbf{P}\boldsymbol{\epsilon}_{\text{opt}}(\mathbf{x})\right)^{\dagger}\left((d(\mathbf{A}(\mathbf{x})))\,\mathbf{s}_{\text{opt}}(\mathbf{x})\right). \tag{19}$$

To simplify (19), define the vector $\mathbf{a}(x) \in \mathbb{R}^{2N_{\text{spec}}}$ as follows.

$$[\mathbf{a}(x)]_m \triangleq \begin{cases} 2\cos(2\pi\nu_m x), & 1 \le m \le N_{\text{spec}}, \\ -2\sin\big(2\pi\nu_{m-N_{\text{spec}}}x\big), & N_{\text{spec}}+1 \le m \le 2N_{\text{spec}}. \end{cases}$$

Also, define the vector $\mathbf{b}(x) \in \mathbb{R}^{2N_{\text{spec}}}$ to be $\mathbf{b}(x) \triangleq \mathbf{a}'(x)$. Then, we have

$$[\mathbf{b}(x)]_m = \begin{cases} (-2\sin(2\pi\nu_m x))\,(2\pi\nu_m), & 1 \le m \le N_{\text{spec}}, \\ \big(2\cos\big(2\pi\nu_{m-N_{\text{spec}}}x\big)\big)\,\big(-2\pi\nu_{m-N_{\text{spec}}}\big), & N_{\text{spec}}+1 \le m \le 2N_{\text{spec}}. \end{cases} \tag{20}$$

Hence, we have the following.

$$\mathbf{A}(\mathbf{x}) = \begin{bmatrix} \mathbf{a}^{T}(x_1) \\ \cdots \\ \mathbf{a}^{T}(x_{N_{\text{IFGM}}}) \end{bmatrix} \Rightarrow d(\mathbf{A}(\mathbf{x})) = \begin{bmatrix} (dx_1)\,\mathbf{b}^{T}(x_1) \\ \cdots \\ (dx_{N_{\text{IFGM}}})\,\mathbf{b}^{T}(x_{N_{\text{IFGM}}}) \end{bmatrix}.$$

Substituting this into (19), it can be shown that we have

$$d(\zeta(\mathbf{x})) = 2 \sum_{k=1}^{N_{\text{IFGM}}} \left[\mathbf{P}\boldsymbol{\epsilon}_{\text{opt}}(\mathbf{x})\right]_k \mathbf{b}^T(x_k)\, \mathbf{s}_{\text{opt}}(\mathbf{x})\, (dx_k)\,. \tag{21}$$

Now define the matrix $\mathbf{B}(\mathbf{x}) \in \mathbb{R}^{N_{\text{IFGM}} \times 2N_{\text{spec}}}$ as follows:

$$\mathbf{B}(\mathbf{x}) \triangleq \begin{bmatrix} \mathbf{b}^T(x_1) \\ \cdots \\ \mathbf{b}^T(x_{N_{\text{IFGM}}}) \end{bmatrix}.$$

Then, from (21) and (17), it can be shown that the gradient $\nabla\zeta(\mathbf{x})$ is given by

$$\nabla\zeta(\mathbf{x}) = 2\left[\mathbf{P}\boldsymbol{\epsilon}_{\text{opt}}(\mathbf{x})\right] \circ \underbrace{\left[\mathbf{B}(\mathbf{x})\, \mathbf{s}_{\text{opt}}(\mathbf{x})\right]}_{\widehat{\mathbf{i}}(\mathbf{x})}, \tag{22}$$

where $\circ$ denotes the *Hadamard product* (i.e., element-wise product). Here, $\widehat{\mathbf{i}}(\mathbf{x})$ can be interpreted as a vector of samples of the derivative of the IFGM, namely $I'_\sigma(x)$, generated using the optimal spectrum $\mathbf{s}_{\text{opt}}(\mathbf{x})$ as a seed or basis vector.

An overview of the algorithm used to compute the gradient of the spectrum-optimized TRP objective $\zeta(\mathbf{x})$ from (16) is shown in Table 2. Note that computation of the gradient vector $\nabla\zeta(\mathbf{x})$ only requires one explicit calculation involving the inverse $\left(\mathbf{A}^\dagger(\mathbf{x})\,\mathbf{P}\mathbf{A}(\mathbf{x}) + \mathbf{Q}\right)^{-1}$, which is required to compute $\mathbf{s}_{\text{opt}}(\mathbf{x})$.

B. Addressing Unknown/Imperfect Sample Locations

The purpose of calculating the gradient $\nabla\zeta(\mathbf{x})$ as outlined in Sec. VI-A was for use in a gradient descent algorithm for *locally* minimizing the spectrum-optimal TRP objective $\zeta(\mathbf{x})$ from (16). This objective $\zeta(\mathbf{x})$ represents a regularized MSE for the spectrum reconstruction as a function of the OPD position vector $\mathbf{x}$, in which the spectrum has already been optimized as a function of $\mathbf{x}$. As such, optimization of $\zeta(\mathbf{x})$ is tantamount to carrying out spectrum reconstruction for the case of unknown OPD sample locations. By using an estimate of the OPD position vector obtained from interpolation of the ICS OPD time series data as an initial condition for the gradient descent algorithm, imperfect OPD position information can be fed in at the start, in hopes of correction as a result of the descent algorithm.

To properly address the generation of such an OPD position vector initial condition, note that this may require truncation of the `SimCLK` IFGM samples to fit within the time epoch spanned by the ICS OPD time series. This is illustrated in Figure 18, where we have the following:

- t_{ICS} : ICS TAI timetag,
- t_{IFGM} : `SimCLK` IFGM timetag,
- F_{ICS} : ICS data sampling frequency (nominally 100 Hz),

Table 2. Overview of algorithm used to calculate the gradient vector of the spectrum-optimized TRP objective $\zeta(\mathbf{x})$ from (16).

Algorithm to compute the gradient vector $\nabla\zeta(\mathbf{x})$:

Inputs:

- $\mathbf{i}$ - vector of IFGM samples,
- $\mathbf{x}$ - vector of optical path difference (OPD) position estimates,
- $\boldsymbol{\nu} \triangleq \left[\begin{array}{ccc} \nu_1 & \cdots & \nu_{N_{\text{spec}}} \end{array} \right]$ - *row* vector of wavenumbers corresponding to the OPD-domain IFGM waveform DFS representation,
- $\mathbf{k} \triangleq 2\pi\boldsymbol{\nu}$ - *row* vector of angular wavenumber values,
- $\mathbf{P}, \mathbf{Q}, \mathbf{s}_0$ - MSE/AP spectrum error weight matrices and AP spectrum target vector.

Methodology:

1. Form the nonuniform inverse discrete Fourier transform matrix $\mathbf{A}(\mathbf{x})$.
2. Calculate the spectrum vector $\mathbf{s}_{\text{opt}}(\mathbf{x}) = \left(\mathbf{A}^{\dagger}(\mathbf{x})\,\mathbf{P}\mathbf{A}(\mathbf{x}) + \mathbf{Q}\right)^{-1}\left(\mathbf{A}^{\dagger}(\mathbf{x})\,\mathbf{P}\mathbf{i} + \mathbf{Q}\mathbf{s}_0\right)$ as in (15).
3. Compute the error vector $\boldsymbol{\epsilon}_{\text{opt}}(\mathbf{x}) = \mathbf{A}(\mathbf{x})\,\mathbf{s}_{\text{opt}}(\mathbf{x}) - \mathbf{i}$ as in (18).
4. Generate the derivative matrix $\mathbf{B}(\mathbf{x})$ using $\mathbf{A}(\mathbf{x})$ and $\mathbf{k}$ using (20).
5. Calculate the IFGM derivative vector $\widehat{\mathbf{i}}(\mathbf{x}) = \mathbf{B}(\mathbf{x})\,\mathbf{s}_{\text{opt}}(\mathbf{x})$ defined in (22).
6. Compute the gradient vector as $\nabla\zeta(\mathbf{x}) = 2\left[\mathbf{P}\boldsymbol{\epsilon}_{\text{opt}}(\mathbf{x})\right] \circ \widehat{\mathbf{i}}(\mathbf{x})$ as in (22).

- F_{IFGM} : `SimCLK` IFGM data sampling frequency (equal to $F_{\text{IFGM,nom}}/L$ as shown in Figure 1),
- N_{ICS} : number of ICS OPD data samples.

Assuming that the nominal number of `SimCLK` IFGM samples is $N_{\text{IFGM,nom}}$, the `SimCLK` IFGM samples will correspond to the following set of times:

$$\left\{ t_{\text{IFGM}} + \frac{k-1}{F_{\text{IFGM}}} \right\}_{k=1}^{N_{\text{IFGM,nom}}} . \tag{23}$$

However, not all of these times may lie in the ICS time epoch described by the following interval:

$$\left[t_{\text{ICS}}, t_{\text{ICS}} + \frac{N_{\text{ICS}} - 1}{F_{\text{ICS}}} \right] . \tag{24}$$

Any `SimCLK` IFGM samples with times from (23) which lie outside of the ICS epoch given by (24) should be excised and not used for reconstruction. A set of `SimCLK`

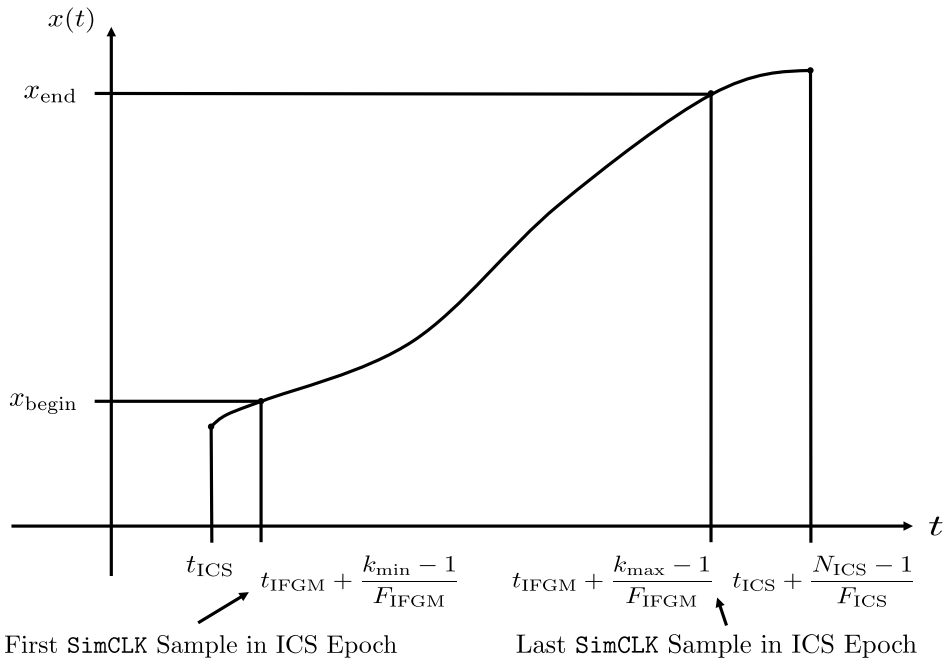

Figure 18. Interfacing the ICS OPD time series and the SimCLK IFGM data.

IFGM sample times that ensures that only the smallest number of samples is excised is as follows:

$$\left\{ t_{\text{IFGM}} + \frac{k-1}{F_{\text{IFGM}}} \right\}_{k=k_{\min}}^{k_{\max}},$$

where $k_{\min}$ and $k_{\max}$ are as shown in Figure 18 and given by

- $k_{\min} = \max(1, \lceil F_{\text{IFGM}}\tau \rceil + 1)$,
- $k_{\max} = \min\Big(N_{\text{IFGM,nom}}, \Big\lfloor F_{\text{IFGM}}\tau + \frac{F_{\text{IFGM}}}{F_{\text{ICS}}}\,(N_{\text{ICS}}-1) \Big\rfloor + 1\Big)$.

Here, $\tau \triangleq t_{\text{ICS}} - t_{\text{IFGM}}$ is the time interval between the ICS and SimCLK IFGM timetags.

C. Incorporating A Priori Spectrum Information to Aid in Reconstruction

Information from previous data captures when the TES laser was operational can be used to formulate a priori statistics to feed into the reconstruction algorithm described here. For a given uncalibrated spectrum type (target (TGT), black-body (BB), or cold space (CS)) and for a given optical band of interest, the mean $\boldsymbol{\mu}_{\mathbf{s}}$ and covariance $\boldsymbol{\Sigma}_{\mathbf{s}}$ of the spectrum can be calculated using laser derived data close in time to the SimCLK run under consideration. Referring back to the original TRP objective from (14), we can incorporate $\boldsymbol{\mu}_{\mathbf{s}}$ and $\boldsymbol{\Sigma}_{\mathbf{s}}$ into the reconstruction algorithm as follows:

$$\mathbf{s}_0 = \boldsymbol{\mu}_{\mathbf{s}}\,,\ \mathbf{Q} = \boldsymbol{\Sigma}_{\mathbf{s}}^{-1}. \tag{25}$$

This approach may be reasonable for spectra that are known not to vary greatly as a function of time, such as the uncalibrated BB, but it may be more susceptible to error

for spectra that are expected to change with time, such as the uncalibrated TGT and CS. Regardless, a priori statistics may be used to help steer the reconstruction toward a nominally acceptable spectrum in an initial run of the algorithm until convergence, after which the algorithm may be run again using the previously converged OPD position vector as an initial condition, but without the a priori statistics being used.

For cases in which it may not be preferable to use a priori statistics to assist in reconstruction, such as when we wish to discover unique features of the spectrum under consideration, it is still worthwhile incorporating fundamental a priori information in the reconstruction. For example, every IFGM waveform is intrinsically an autocorrelation type signal [2], meaning that, when centered at the ZPD, will ideally lead to a spectrum that is both real and non-negative. Furthermore, every IFGM waveform captured from TES is filtered using an optical bandpass filter, for which the band edges are all known in advance. Use of such a priori information in the reconstruction problem will regularize the resulting spectrum, preventing ill-conditioned solutions such as those seen in Sec. III from manifesting.

One way to incorporate this fundamental a priori information into the TRP reconstruction algorithm is to select $\mathbf{s}_0$ and $\mathbf{Q}$ to penalize the out-of-band (OOB) energy, as well as the energy of the imaginary part of the spectrum. Practically, this requires that the IFGM has been approximately centered at the ZPD, which can be done coarsely by centering the IFGM vector at the sample corresponding the maximum absolute value, i.e., by having the maximum absolute value IFGM sample correspond to $x = 0$. To penalize the OOB/imaginary energy of the spectrum, $\mathbf{s}_0$ and $\mathbf{Q}$ can be chosen as follows:

$$\mathbf{s}_0 = \mathbf{0}_{2N_{\text{spec}}\times 1}\,,\ \mathbf{Q} = \mathbf{\Lambda}_{\text{OOB/I}}. \tag{26}$$

Here, $\mathbf{\Lambda}_{\text{OOB/I}}$ is a matrix that penalizes both the OOB/imaginary energy of the spectrum and is given by

$$\mathbf{\Lambda}_{\text{OOB/I}} \triangleq \begin{bmatrix} \mathbf{\Lambda}_{\text{OOB,R}} & \mathbf{0}_{N_{\text{spec}}\times N_{\text{spec}}} \\ \mathbf{0}_{N_{\text{spec}}\times N_{\text{spec}}} & \mathbf{\Lambda}_{\text{I}} \end{bmatrix},$$

where $\mathbf{\Lambda}_{\text{OOB,R}}$ penalizes the real part of the OOB energy and is defined as

$$\mathbf{\Lambda}_{\text{OOB,R}} \triangleq \begin{bmatrix} \mathbf{I}_{N_{\text{OOB,L}}} & \mathbf{0}_{N_{\text{OOB,L}}\times N_{\text{IB}}} & \mathbf{0}_{N_{\text{OOB,L}}\times N_{\text{OOB,U}}} \\ \mathbf{0}_{N_{\text{IB}}\times N_{\text{OOB,L}}} & \mathbf{0}_{N_{\text{IB}}\times N_{\text{IB}}} & \mathbf{0}_{N_{\text{IB}}\times N_{OOB,U}} \\ \mathbf{0}_{N_{\text{OOB,U}}\times N_{\text{OOB,L}}} & \mathbf{0}_{N_{\text{OOB,U}}\times N_{\text{IB}}} & \mathbf{I}_{N_{\text{OOB,U}}} \end{bmatrix},$$

while $\mathbf{\Lambda}_{\text{I}}$ penalizes the imaginary part of the spectrum energy and is given by

$$\mathbf{\Lambda}_{\text{I}} \triangleq \mathbf{I}_{N_{\text{spec}}}.$$

The quantities $N_{\text{OOB,L}}$, N_{IB}, and $N_{\text{OOB,U}}$ denote the number of spectrum indices that lie in the lower OOB, in-band (IB), and upper OOB regions, respectively.

It should be noted that while the choices of $\mathbf{s}_0$ and $\mathbf{Q}$ given by (26) penalize the OOB/imaginary energy of the reconstructed spectrum, they do not necessarily

encourage solutions with non-negative real parts, as desired here. This is because this additional constraint would make the original problem of minimizing $\xi(\mathbf{x}, \mathbf{s})$ from (14) a quadratic programming (QP) problem [4] in terms of $\mathbf{s}$, rendering joint optimization of the spectrum $\mathbf{s}$ and position vector $\mathbf{x}$ as carried out in Sec. VI difficult if not impossible. Instead, we relied on using (26) in hopes that a non-negative real spectrum solution was obtained, or considered using (25) followed by (26) in order to yield a spectrum solution which either entirely or approximately had a non-negative real part.

D. Spectrum Reconstruction Example Incorporating A Priori Information

We considered spectrum reconstruction for the following `SimCLK` IFGM data:

- Run ID: 27710,
- Spectrum Type: BB,
- Scan ID: 02,
- Filter ID: 1B2,
- Pixel ID: 07.

Before applying the data to the unknown sample location (USL) TRP spectrum reconstruction (SR) algorithm described in Sec. VI-A, a smoothing pre-processing stage in the IFGM raw spectral domain was carried out to remove spikes due to direct current (DC) offset and ADC sampling artifacts. For this, we utilized a robust local regression technique using weighted linear least squares and a 2nd degree polynomial model to smooth out the spikes in the magnitude spectrum. The span of the smoothing window in this case was set to 11 samples.

The EP output of the ICS data file corresponding to the `SimCLK` run was used to generate an OPD time series, from which the initial position vector $\mathbf{x}_0$ was derived. This was implemented as described below:

- The resulting OPD time series was generated by PCHIP interpolation of the knot points.
- The TAI timetags from the ICS/`SimCLK` data files were set to correspond to the first OPD time series sample and first IFGM sample, respectively.
- ICS/`SimCLK` timing was aligned, and the IFGM samples outside of the ICS epoch were truncated, as described in Sec. VI-B (see Figure 18 for more details).
- The OPD time series positions corresponding to `SimCLK` sample times were taken to be the initial position vector $\mathbf{x}_0$.

To reduce the computational overhead of the USL TRP algorithm, we carried out simulations on an IFGM data window of length $N_{\mathrm{IFGM}} = 1024$ centered near the ZPD.

Specifically, this meant that the IFGM was truncated to 1024 samples with the maximum absolute value IFGM sample occurring at one of the middle points of the window (in this case, the 513-th sample). To make the reconstruction problem well-posed and full, we took $N_{\text{spec}} = 512$.

For the USL TRP algorithm, the parameters were chosen to minimize a convex combination [4] of MSE and OOB/imaginary energy. To that end, a trade-off parameter θ satisfying $\theta \in [0, 1]$ was considered. Specifically, $\mathbf{P}$, $\mathbf{Q}$, and $\mathbf{s}_0$ were chosen as follows:

- $\mathbf{P} = \theta \mathbf{I}_{N_{\text{IFGM}}}$,
- $\mathbf{Q} = (1 - \theta)\, \mathbf{\Lambda}_{\text{OOB/I}}$,
- $\mathbf{s}_0 = \mathbf{0}_{2N_{\text{spec}} \times 1}$.

We implemented a gradient descent algorithm on the position vector $\mathbf{x}$ as described in Table 2 using a constant step-size γ. From the evolution of this algorithm, a refined OPD time series was formulated based on sample times corresponding to `SimCLK` IFGM values and the USL TRP spectrum reconstruction algorithm position vector output $\mathbf{x}$. The specific USL TRP parameters chosen here were as follows:

- $\theta = 0.01$,
- OOB lower/upper limit wavenumber values used were $\nu_{\text{OOB,L}} = 900$ cm^{-1} and $\nu_{\text{OOB,U}} = 1210$ cm^{-1}, respectively,
- $\gamma = 10^{-14}$,
- number of iterations N_{iter} considered was $N_{\text{iter}} = 30000$.

Plots of the magnitude/phase of the initial and final spectra output from the USL TRP SR algorithm are shown in Figure 19(a) and (b), respectively, along with the raw spectrum of the IFGM sample vector. Compare these results with the expected 1B2 BB spectrum magnitude and phase shown in Figure 20(a) and (b), respectively.

As can be seen, the reconstructed spectrum bears some resemblance to the desired BB shape, although the reconstruction is arguably unsatisfactory. In particular, though, note that the magnitudes for the OOB regions, due to the optical bandpass filter, are suppressed as desired. Furthermore, the notch in the 1B2 BB spectrum near $\nu = 1115$ cm^{-1} (see Figure 20(a)) can be seen to manifest as shown in the final spectrum magnitude shown in Figure 19(a). From Figure 19(b), it is clear that the output spectrum has a phase that is either approximately 0 or $\pm\pi$, meaning that the algorithm is successfully suppressing the imaginary energy of the spectrum as desired. Comparison of Figure 19(b) with Figure 20(b) shows relatively good agreement in the IB region. From Figure 19(b), it can be concluded that the algorithm can be used for phase alignment to the ZPD.

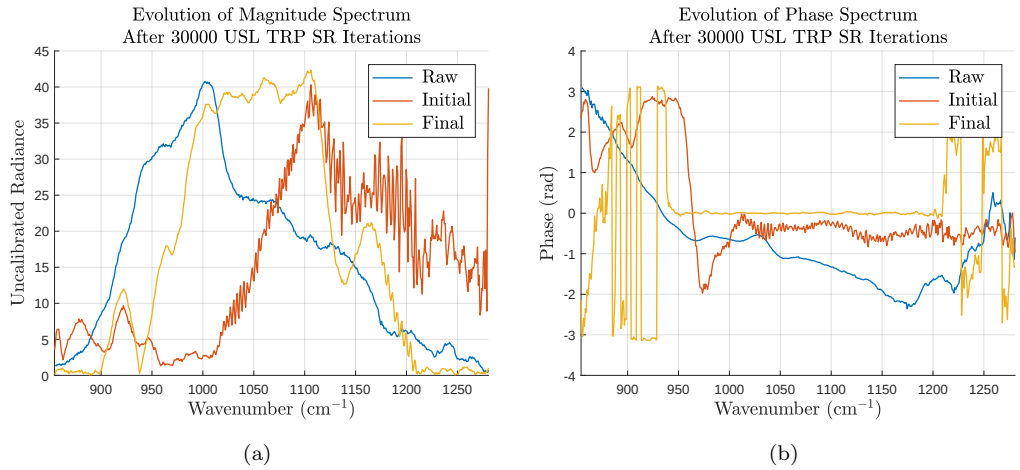

Figure 19. Evolution of the spectrum from the unknown sample location (USL) Tikhonov regularization problem (TRP) spectrum reconstruction (SR) algorithm: (a) magnitude spectrum and (b) phase spectrum.

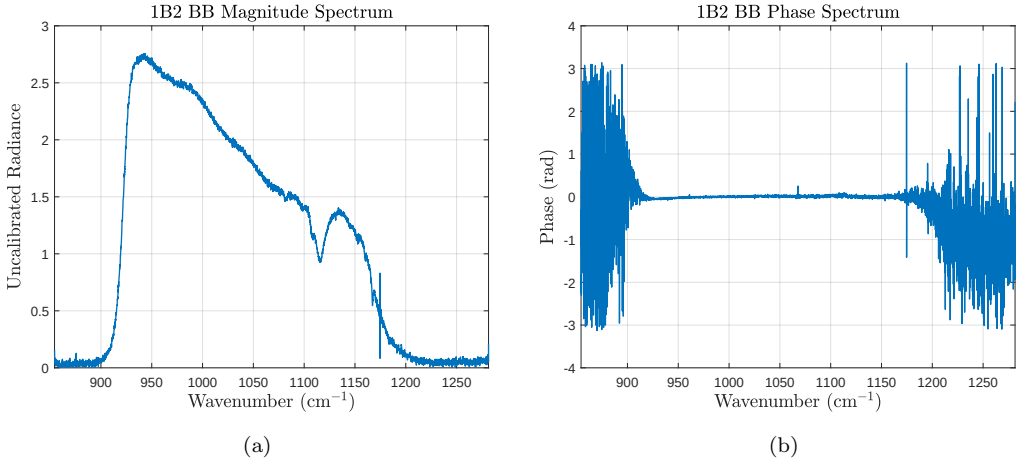

Figure 20. Expected 1B2 BB spectrum: (a) magnitude spectrum and (b) phase spectrum. (Data taken from laser data capture - run ID: 27717, scan ID: 01, pixel ID: 07.)

Using the OPD positions as estimated by the USL TRP algorithm to generate OPD time series based on the `SimCLK` IFGM sample times yielded the velocity and residual position series shown in Figure 21(a) and (b), respectively. From this figure, it is apparent that the velocity profile yielded erratic behavior, while the residual position appeared well behaved. One likely reason for the erratic behavior in the velocity from Figure 21(a) is that perturbations in the OPD position vector $\mathbf{x}$ as a result of the algorithm occur over the `SimCLK` IFGM sample time interval, which is much smaller than the ICS sample time interval, by over an order of magnitude. As such, this suggests that the resulting velocity profile of the OPD time series generated by the algorithm may not be a useful measure to characterize the ability of the algorithm to yield a physically realizable OPD time series. A better measure to gauge a physically realizable OPD time series would be the residual position, as shown in Figure 21(b).

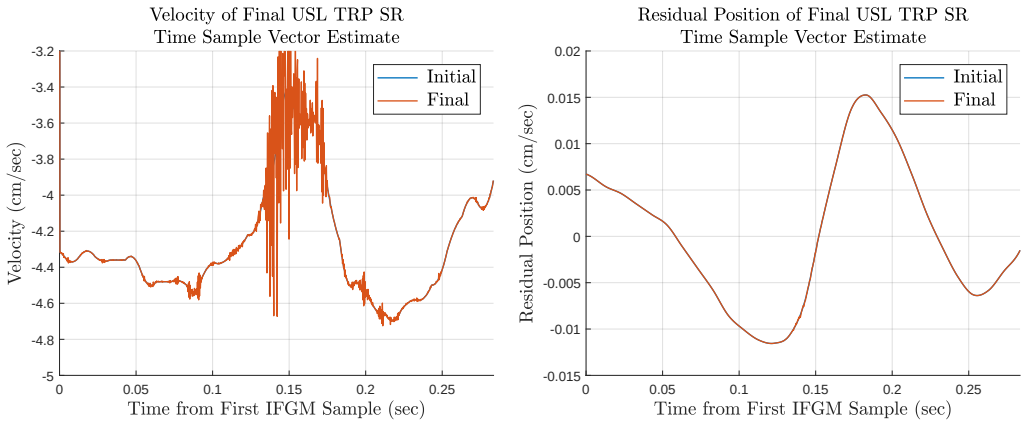

Figure 21. OPD time series generated using the position vector estimates returned from the USL TRP algorithm along with the `SimCLK` IFGM sample times: (a) velocity and (b) residual position.

From this, it can be seen that an OPD position vector change leading to a virtually indistinguishable residual position time series can yield a vastly different spectrum, as evidenced in Figure 19.

Because of the similarity between the initial and final USL TRP algorithm OPD residual position time series, a plot of the difference between the final and initial OPD time series is given in Figure 22, in order to highlight the evolution of the algorithm. From this figure, several interesting observations can be made. First, most of the noticeable content of the difference signal occurs near the middle of the observation epoch, which was chosen to correspond roughly with the position of the ZPD. This is in line with intuition, as most of the corrections in the reconstruction of the spectrum should occur where the energy of the IFGM is most concentrated, which is the ZPD region for uncalibrated BB spectra (see Figure 17).

Another observation which can be made from Figure 22 is that the magnitude of the OPD position vector perturbations is on the order of several microns. Specifically, the range of perturbations is approximately 5×10^{-4} cm, which is roughly half of the period of the local variations of the IFGM waveform of 9.36452×10^{-4} cm as given in (13). Note that this is consistent with the observation from Figure 17 that any perturbation of the sample positions near the ZPD that is on the order of microns can lead to vastly different IFGM amplitude values.

Finally, the evolution of the USL TRP cost function $\zeta(\mathbf{x})$ given in (16) across iterations is shown in Figure 23. As can be seen, the cost function decreases monotonically at each iteration, due to the small step-size value of $\gamma = 10^{-14}$ chosen here. Furthermore, it can be see that after $N_{\text{iter}} = 30000$ iterations, the TRP cost function $\zeta(\mathbf{x})$ appears to have approached an asymptotic value, suggesting that the algorithm has approximately converged.

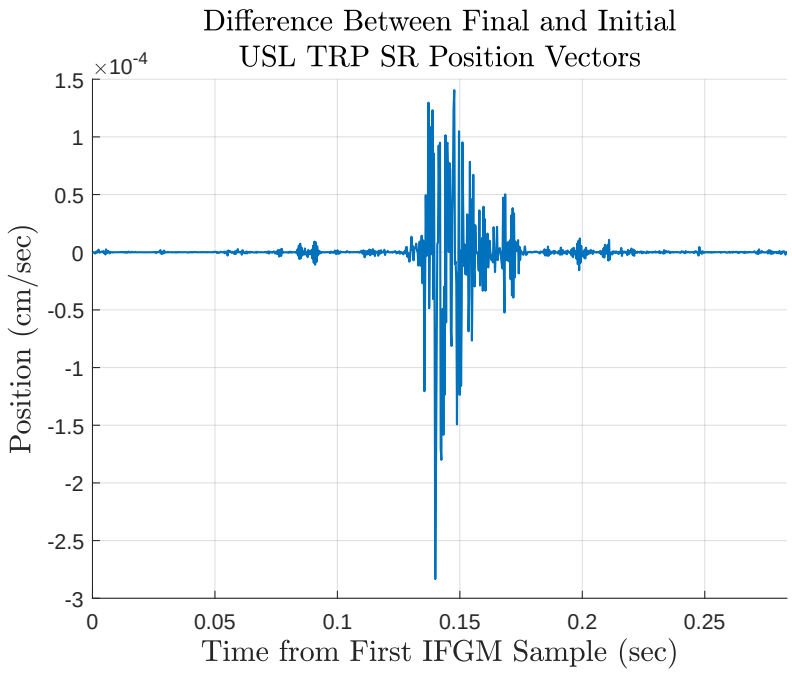

Figure 22. Difference between final and initial OPD time series obtained via the USL TRP SR algorithm.

VII. Unknown/Imperfect Sample Location Power Spectral Density Spectrum Reconstruction

In theory, the IFGM waveform $I(x)$ introduced in Sec. II should be an *autocorrelation* function [2], as it measures how much the light intensity of a tropospheric source interferes with itself as a function of the OPD. As discussed below, this can aid in making the spectrum reconstruction problem more well-conditioned, as it implies that the IFGM signal is *Hermitian symmetric*, i.e., $I(-x) = I^*(x)$ for all x [2]. (Specifically, as $I(x)$ is real here, Hermitian symmetry implies that the IFGM waveform is even, i.e., $I(-x) = I(x)$ for all x.) A necessary and sufficient condition for $I(x)$ to be an autocorrelation function is that its Fourier transform $S(\nu)$ is non-negative for all ν, i.e., $S(\nu) \geq 0$ for all ν [2]. In this case, $S(\nu)$ is called a power spectral density (PSD) [2].

In accordance with the DFS representation of $I_\sigma(x)$ from Sec. II, this implies that $I(x)$ can be modeled by a DFS representation of the form

$$I(x) = \sum_{m=1}^{N_{\text{spec}}} 2\cos(2\pi\nu_m x)\, s_m, \tag{27}$$

where the set of wavenumbers $\{\nu_m\}_{m=1}^{N_{\text{spec}}}$ is as given in (1). With this representation, $I(x)$ is an autocorrelation function if and only if $s_m \geq 0$ for all m. A more compact form of $I(x)$ from (27) is given by

$$I(x) = \mathbf{c}^T(x)\,\mathbf{s}, \tag{28}$$

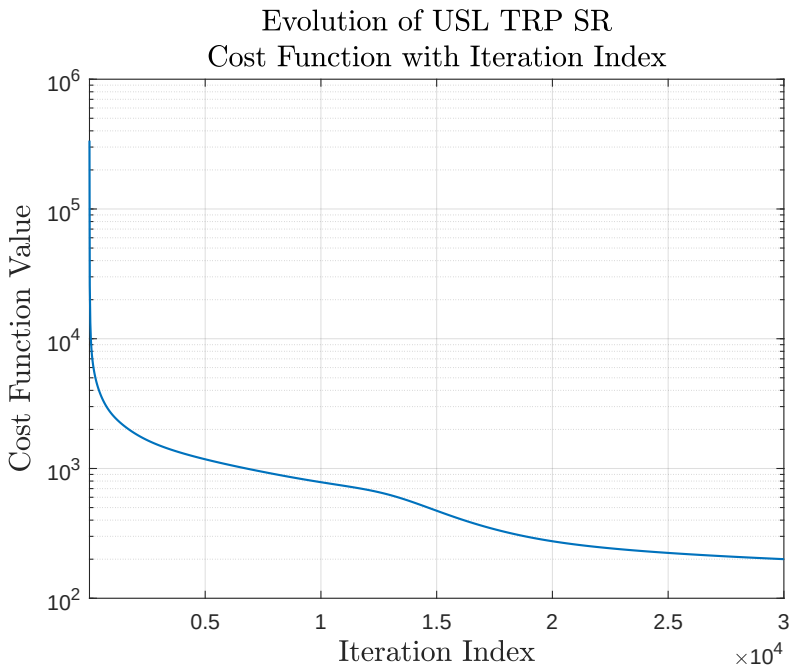

Figure 23. Evolution of the USL TRP SR cost function $\zeta(\mathbf{x})$ from (16) with iteration index. ($\theta = 0.01$, $\gamma = 10^{-14}$, $N_{\text{iter}} = 30000$)

where we have

$$\mathbf{c}(x) \triangleq \begin{bmatrix} 2\cos(2\pi\nu_1 x) \\ \cdots \\ 2\cos\big(2\pi\nu_{N_{\text{spec}}} x\big) \end{bmatrix} \in \mathbb{R}^{N_{\text{spec}}}, \; \mathbf{s} \triangleq \begin{bmatrix} s_1 \\ \cdots \\ s_{N_{\text{spec}}} \end{bmatrix} \in \mathbb{R}^{N_{\text{spec}}}. \tag{29}$$

To use the autocorrelation representation of $I(x)$ in (28) for spectrum reconstruction, from the definitions given in (29), it follows that we must enforce the constraint that $\mathbf{s} \succeq \mathbf{0}$ (i.e., we must constrain $\mathbf{s}$ to be component-wise non-negative) [4].

A. Objective for USL PSD Spectrum Reconstruction

Given a set of `SimCLK` IFGM samples $\{I_k\}_{k=1}^{N_{\text{IFGM}}}$, and using the IFGM waveform representation from (28), one suitable cost function to minimize in the unknown/imperfect sample location scenario is the residual sum of squares (RSS) plus a logarithmic barrier penalty on adjacent sample spacings [5]:

$$\xi(\mathbf{x}, \mathbf{s}) \triangleq ||\mathbf{i} - \mathbf{C}(\mathbf{x})\,\mathbf{s}||^2 + \mu \sum_{k=2}^{N_{\text{IFGM}}} P(x_k - x_{k-1}), \tag{30}$$

where we have

$$\begin{aligned}
[\mathbf{i}]_k &\triangleq I_k\,,\ 1 \le k \le N_{\text{IFGM}}\,,\\
[\mathbf{x}]_k &\triangleq x_k\,,\ 1 \le k \le N_{\text{IFGM}}\,,\\
[\mathbf{C}(\mathbf{x})]_{k,m} &\triangleq \left[\mathbf{c}^T(x_k)\right]_m = 2\cos(2\pi\nu_m x_k)\,,\ 1 \le k \le N_{\text{IFGM}}\,,\ 1 \le m \le N_{\text{spec}}\,,\\
[\mathbf{s}]_m &\triangleq s_m\,,\ 1 \le m \le N_{\text{spec}}\,,\\
P(\Delta x) &\triangleq \Delta x - \log(\Delta x - \alpha) - \log(\beta - \Delta x)\ .
\end{aligned}$$

Here, the parameters μ, α, and β represent the following:

- μ - weighting parameter for the logarithmic barrier penalty term on adjacent sample spacings,
- α, β - lower/upper limit, respectively, on any adjacent sample spacing Δx (i.e., $\alpha < \Delta x < \beta$).

The RSS component in $\xi(\mathbf{x}, \mathbf{s})$ from (30) is a model fitting term, while the logarithmic barrier penalty term can be used to ensure that physically realizable OPD time series solutions will result. Use of this type of penalty term for spectrum reconstruction in the case of unknown sample locations was first considered by Browning in [5].

As mentioned earlier, one major advantage to modeling $I(x)$ as an autocorrelation function (or equivalently $S(\nu)$ as a PSD) is that it makes the reconstruction problem more well-conditioned. As opposed to nonuniform sampling near the Nyquist rate, ensuring $I(x)$ is even means that this sampling will occur at approximately *twice* the Nyquist rate. This well-conditioning manifests in the reduced condition number [3] of the matrix $\mathbf{C}(\mathbf{x})$ from (30) compared with the matrix $\mathbf{A}(\mathbf{x})$ from (4). (Recall that the condition number of any matrix is defined to be the ratio of the maximum singular value to the minimum singular value [3].)

An example of this is shown in Figure 24, where we have plotted the singular values of $\mathbf{C}(\mathbf{x})$ using the same data used to form the matrix $\mathbf{A}(\mathbf{x})$ in Figure 3. In this case, $\mathbf{C}(\mathbf{x})$ was found to be of full rank. Specifically, for the same set of data, the condition number for $\mathbf{C}(\mathbf{x})$ was 20.9918, compared with that of $\mathbf{A}(\mathbf{x})$, which was 2.8644×10^{12}. It should be noted that the benefit of modeling $I(x)$ as an autocorrelation function, in terms of making the spectrum reconstruction problem more well-conditioned, comes at the cost of ensuring that $\mathbf{s} \succeq \mathbf{0}$.

B. Approach for USL PSD Cost Function Optimization

As joint optimization of the position and spectrum vectors ($\mathbf{x}$ and $\mathbf{s}$, respectively) in the objective from (30) appears intractable, in contrast to the Tikhonov regularized problem from Sec. VI, the method considered here is to optimize each, assuming the other is fixed. This approach is essentially the alternating least squares (ALS) method considered by Browning [5].

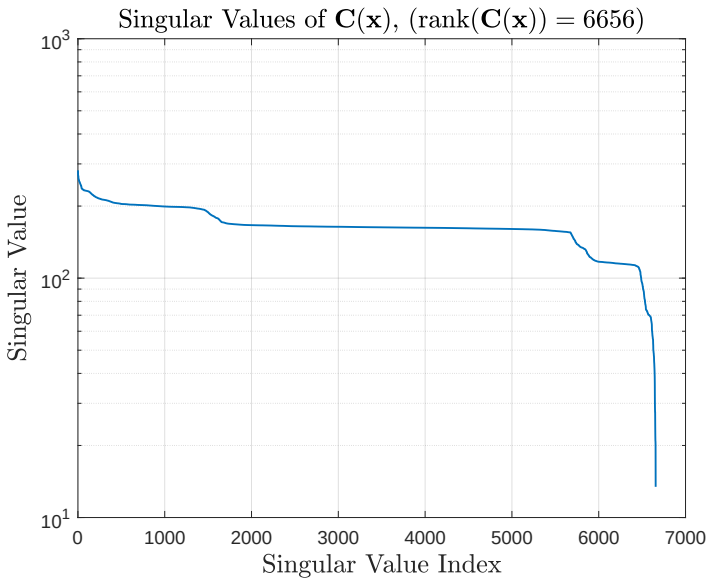

Figure 24. Singular values of the matrix $\mathbf{C}(\mathbf{x})$ for a 1B2 black-body (BB) scan. ($N_{\text{IFGM}} = 14085$, $N_{\text{spec}} = 6656$)

To that end, we define the following quantities:

- $\zeta_{\mathbf{s}}(\mathbf{x}) \triangleq \xi(\mathbf{x}, \mathbf{s})$ - cost function with variable $\mathbf{x}$ and fixed $\mathbf{s}$,
- $\eta_{\mathbf{x}}(\mathbf{s}) \triangleq \xi(\mathbf{x}, \mathbf{s})$ - cost function with variable $\mathbf{s}$ and fixed $\mathbf{x}$.

The problem of minimizing the objective $\zeta_{\mathbf{s}}(\mathbf{x})$ is non-linear and non-convex [4] in terms of $\mathbf{x}$ and is optimized here via *gradient descent*. Subject to the constraint $\mathbf{s} \succeq \mathbf{0}$, the problem of optimizing $\eta_{\mathbf{x}}(\mathbf{s})$ can be posed as a quadratic programming (QP) problem [4], which is non-linear, but *convex*. Such problems can be optimized *globally* using interior-point methods [4]. For example, in MATLAB, such problems, along with several other convex optimization problems, can be solved using the freely available add-on CVX [6].

With $\mathbf{x}$ and $\mathbf{s}$ optimized as described above, the process is repeated until convergence occurs. In all cases considered here, convergence was always achieved and conjectured to correspond to a locally optimal solution.

1. USL PSD Cost Function Position Gradient Vector

The gradient of $\zeta_{\mathbf{s}}(\mathbf{x})$, namely $\nabla\zeta_{\mathbf{s}}(\mathbf{x})$, can be shown to be the following:

$$[\nabla\zeta_{\mathbf{s}}(\mathbf{x})]_k = \begin{cases} [\mathbf{r}(\mathbf{x}) \circ \mathbf{h}(\mathbf{x})]_k + \mu\left[-1 + \frac{1}{x_{k+1}-x_k-\alpha} - \frac{1}{\beta-x_{k+1}+x_k}\right], & k = 1, \\ [\mathbf{r}(\mathbf{x}) \circ \mathbf{h}(\mathbf{x})]_k + \mu\left[\frac{1}{x_{k+1}-x_k-\alpha} - \frac{1}{\beta-x_{k+1}+x_k} - \frac{1}{x_k-x_{k-1}-\alpha} + \frac{1}{\beta-x_k+x_{k-1}}\right], & 2 \leq k \leq N_{\text{IFGM}}-1, \\ [\mathbf{r}(\mathbf{x}) \circ \mathbf{h}(\mathbf{x})]_k + \mu\left[1 - \frac{1}{x_k-x_{k-1}-\alpha} + \frac{1}{\beta-x_k+x_{k-1}}\right], & k = N_{\text{IFGM}}. \end{cases}$$

Here, we have

- $\mathbf{r}(\mathbf{x}) \triangleq \mathbf{i} - \mathbf{C}(\mathbf{x})\,\mathbf{s}$: residual vector,
- $\mathbf{h}(\mathbf{x}) \triangleq \mathbf{D}(\mathbf{x})\,\mathbf{s}$: scaled IFGM derivative vector,
- $[\mathbf{D}(\mathbf{x})]_{k,m} \triangleq 8\pi\nu_m \sin(2\pi\nu_m x_k)$: (k,m)-th element of the derivative matrix $\mathbf{D}(\mathbf{x})$,
- $\circ$: Hadamard product operator (i.e., element-wise product).

For gradient descent, given a current position/spectrum vector pair $(\mathbf{x}, \mathbf{s})$, a position vector update $\mathbf{x}^+$ is calculated as follows:

$$\mathbf{x}^+ = \mathbf{x} - \gamma \nabla \zeta_{\mathbf{s}}(\mathbf{x})\,,$$

where γ is the step-size parameter. Here, γ was set via backtracking line search (BLS) [4] based on the Armijo-Goldstein condition, and to ensure that the adjacent spacing condition $\alpha < \Delta x < \beta$ was not violated.

2. USL PSD Cost Function Quadratic Programming Problem for the Spectrum Vector

For fixed position vector $\mathbf{x}$, the problem of finding the spectrum vector $\mathbf{s}$ can be expressed as:

$$\begin{aligned} &\text{minimize} \quad \eta_{\mathbf{x}}(\mathbf{s}) = \mathbf{s}^T \mathbf{Q}(\mathbf{x})\,\mathbf{s} + \mathbf{p}^T(\mathbf{x})\,\mathbf{s} + c(\mathbf{x})\,, \\ &\text{subject to} \quad \mathbf{s} \succeq \mathbf{0}. \end{aligned} \tag{31}$$

Here, we have the following:

- $\mathbf{Q}(\mathbf{x}) \triangleq \mathbf{C}^T(\mathbf{x})\,\mathbf{C}(\mathbf{x})$ (which satisfies $\mathbf{Q}(\mathbf{x}) \succeq \mathbf{0}$, i.e., $\mathbf{Q}(\mathbf{x})$ is *positive semidefinite*),
- $\mathbf{p}(\mathbf{x}) \triangleq -2\mathbf{C}^T(\mathbf{x})\,\mathbf{i}$,
- $c(\mathbf{x}) \triangleq \mathbf{i}^T\mathbf{i} + \mu \sum_{k=2}^{N_{\text{IFGM}}} P(x_k - x_{k-1})$.

Note that (31) is an instance of the general *convex* quadratic programming (QP) problem described below in Table 3. As stated earlier, the convex QP for finding $\mathbf{s}$ can be optimized globally using CVX in MATLAB [6].

C. Algorithm for Solving the USL PSD Spectrum Reconstruction Problem

The methodology behind minimizing the cost function objective $\xi(\mathbf{x}, \mathbf{s})$ given in (30) is shown below in Table 4. Regarding this approach, care must be taken in terms of selecting $\mathbf{x}^{(1)}$ so that the ZPD location of the IFGM waveform $I(x)$ corresponds approximately to $x = 0$. Provided the cost $\xi\big(\mathbf{x}^{(p+1)}, \mathbf{s}^{(p)}\big)$ from Step 1 of Table 4 decreases, then $\xi\big(\mathbf{x}^{(p+1)}, \mathbf{s}^{(p+1)}\big)$ is non-increasing and bounded below (by zero), and so converges [4] (possibly to a local minimum).

Table 3. General form of a convex quadratic programming (QP) problem [4].

Convex Quadratic Programming (QP) Problem:

$$\begin{aligned} \text{minimize} \quad & (1/2)\,\mathbf{y}^T\mathbf{P}\mathbf{y} + \mathbf{q}^T\mathbf{y} + r, \\ \text{subject to} \quad & \mathbf{G}\mathbf{y} \preceq \mathbf{h}, \\ & \mathbf{A}\mathbf{y} = \mathbf{b}, \\ \text{where} \quad & \mathbf{P} \succeq \mathbf{0}. \end{aligned}$$

Table 4. Overview of alternating position/spectrum vector optimization algorithm used to minimize the cost function $\xi(\mathbf{x}, \mathbf{s})$ from (30).

Unknown/Imperfect Sample Location PSD Spectrum Reconstruction Algorithm:

Let $\mathbf{x}^{(p)}$, $\mathbf{s}^{(p)}$, and $\gamma^{(p)}$ denote the p-th iteration of $\mathbf{x}$, $\mathbf{s}$, from Sec. VII-A and γ from Sec. VII-B.1, respectively, for $p \geq 1$.

Initialization:

- Set $\mathbf{x}^{(1)}$ to some value (say, based on an ICS OPD time series). Compute $\mathbf{s}^{(1)}$ by solving the QP corresponding to $\eta_{\mathbf{x}^{(1)}}(\mathbf{s})$ as in Sec. VII-B.2. Calculate $\xi\big(\mathbf{x}^{(1)}, \mathbf{s}^{(1)}\big)$ and store $\mathbf{x}^{(1)}$, $\mathbf{s}^{(1)}$, and $\xi\big(\mathbf{x}^{(1)}, \mathbf{s}^{(1)}\big)$ for future reference.

Iteration: For $p \geq 1$, do the following:

1. *Position Vector Update (Gradient Descent)* - Calculate $\mathbf{x}^{(p+1)} = \mathbf{x}^{(p)} - \gamma^{(p)} \nabla \zeta_{\mathbf{s}^{(p)}}\big(\mathbf{x}^{(p)}\big)$ as described in Sec. VII-B.1, where the step-size $\gamma^{(p)}$ is selected via BLS and to ensure $\alpha < \Delta x < \beta$.
2. *Spectrum Vector Update (Quadratic Programming)* - Calculate $\mathbf{s}^{(p+1)}$ by solving the QP corresponding to $\eta_{\mathbf{x}^{(p+1)}}(\mathbf{s})$ as described in Sec. VII-B.2.
3. *Store Diagnostics* - Compute $\xi\big(\mathbf{x}^{(p+1)}, \mathbf{s}^{(p+1)}\big)$. Store $\mathbf{x}^{(p+1)}$, $\mathbf{s}^{(p+1)}$, $\xi\big(\mathbf{x}^{(p+1)}, \mathbf{s}^{(p+1)}\big)$, $\nabla \zeta_{\mathbf{s}^{(p)}}\big(\mathbf{x}^{(p)}\big)$, and $\gamma^{(p)}$ for future reference. Increment p to $p \leftarrow p + 1$ and go to Step 1.

D. Spectrum Reconstruction Example

The unknown/imperfect sample location PSD spectrum reconstruction algorithm was tested using the same setup considered in Sec. VI-D. In particular, the following was used here.

- Considered spectrum reconstruction for the following `SimCLK` IFGM data:
  - Run ID: 27710, Spectrum Type: BB, Scan ID: 02, Filter ID: 1B2, Pixel ID: 07.
  - Assumed TAI timetag from `SimCLK` data file corresponded to the first IFGM sample.

- Carried out smoothing pre-processing stage in the IFGM raw spectral domain to remove spikes due to DC offset and ADC sampling artifacts.
  - Utilized a robust variant of local regression using weighted linear least squares and a 2nd-degree polynomial model to smooth out spikes in the magnitude spectrum.
  - Set the span of the smoothing window to 11 samples.
- Used the EP output of the ICS data file to generate an OPD time series, from which the initial position vector was derived.
  - Resulting OPD time series generated by piecewise PCHIP interpolation of the knot points.
  - Assumed TAI timetag from ICS data file corresponded to first OPD time series sample.
  - Aligned ICS/`SimCLK` timing and truncated IFGM samples outside of ICS epoch as described in Figure 18.
  - Took OPD time series positions corresponding to the `SimCLK` sample times to be the initial position vector $\mathbf{x}$.

Regarding the IFGM data window and number of spectral values to use, the following was considered here.

- Simulations were carried out on an IFGM data window of length $N_{\text{IFGM}} = 1024$ centered near the ZPD.
- The largest absolute value IFGM sample was made to correspond to the location $x = 0$.
- Took $N_{\text{spec}} = 512$ in order to make the reconstruction problem well posed and full.

For the unknown/imperfect sample location PSD spectrum reconstruction algorithm, the following parameter values were chosen.

- $\mu = 100$,
- $\alpha = v_{\text{LB}} F_{\text{IFGM}}$, $\beta = v_{\text{UB}} F_{\text{IFGM}}$, where
  - $v_{\text{LB}} = -5$ cm/sec was the OPD velocity lower bound,
  - $v_{\text{UB}} = -3.2$ cm/sec was the OPD velocity upper bound,
  - F_{IFGM} was the `SimCLK` IFGM sample rate.
- $\gamma_{\text{nom}} = 10^{-4}$ (BLS nominal step-size parameter [4]),
- $c = 1/2$ (BLS nominal relative increment level control parameter [4]),
- $\tau = 1/2$ (BLS step-size attenuation factor control parameter [4]).

Plots of the magnitude/phase of the initial and final spectra output from the USL PSD SR algorithm are shown in Figure 25(a) and (b), respectively, along with the raw spectrum of the IFGM sample vector. These results should be compared with the expected 1B2 BB spectrum magnitude and phase shown in Figure 20(a) and (b), respectively.

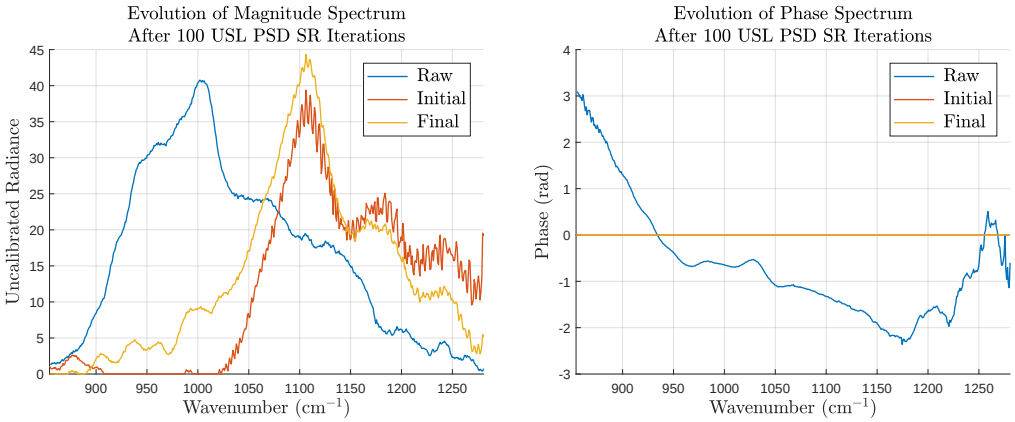

(a) (b)

Figure 25. Evolution of the spectrum from the unknown sample location (USL) power spectral density (PSD) spectrum reconstruction (SR) algorithm: (a) magnitude spectrum and (b) phase spectrum.

As is evident from Figures 25 and 20, while the reconstructed spectrum bears some resemblance to the desired BB shape, the reconstruction is arguably unsatisfactory. However, the algorithm can be seen to be learning to suppress the OOB regions due to the optical bandpass filter. In addition, the known notch in the 1B2 BB spectrum near $\nu = 1120$ cm^{-1} may be manifesting as well. Finally, as desired, the output spectrum has exactly zero phase and thus is non-negative, meaning it is a PSD.

Using the OPD positions estimated by the USL PSD algorithm, an OPD time series based on the `SimCLK` IFGM sample times yielded the velocity and residual position series shown in Figure 26(a) and (b), respectively. As can be seen, the velocity time series was relatively smooth, outside of an isolated erratic region near the occurrence of the ZPD. While difficult to visualize from Figure 26(a), the velocity profile just barely missed the OPD velocity upper bound of $v_{\mathrm{UB}} = -3.2$ cm/sec. In contrast to the velocity, the residual position from Figure 26(b) is very smooth and only exhibits slight perturbations near the ZPD leading to velocity spikes.

A plot of the difference between the final and initial OPD time series is given in Figure 27, in order to highlight the evolution of the algorithm. As with the case for the USL TRP algorithm, it can be seen from this figure that most of the activity in the difference signal occurred near the middle of the observation epoch, corresponding approximately with the position of the ZPD. Also, the difference between final and initial position vectors is on the order of microns, which emphasizes the fact that small changes in the position vector can lead to large differences in the output reconstructed spectrum.

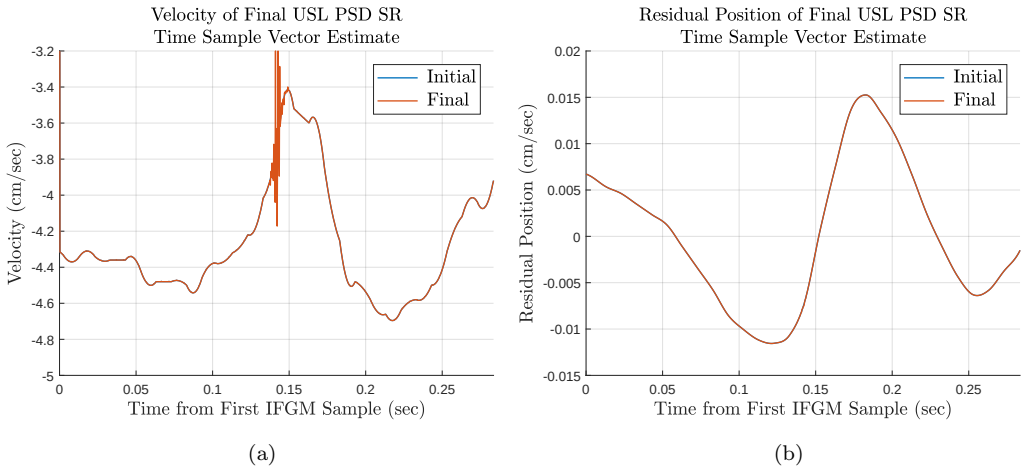

Figure 26. OPD time series generated using the position vector estimates returned from the USL PSD algorithm along with the `SimCLK` IFGM sample times: (a) velocity and (b) residual position.

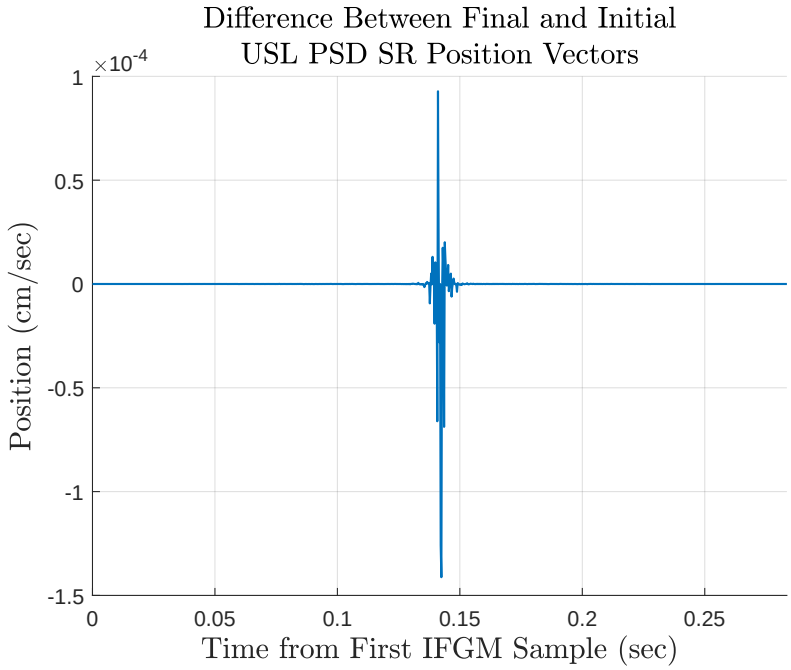

Figure 27. Difference between final and initial OPD time series obtained via the USL PSD SR algorithm.

Finally, the evolution of the USL PSD SR cost function $\xi(\mathbf{x}, \mathbf{s})$ given in (30) and the step-size parameter γ from Sec. VII-B.1 across iterations is shown in Figure 28(a) and (b), respectively. As can be seen from Figure 28(a), the cost function decreased monotonically at each iteration, which is a consequence of the BLS taken in the position vector gradient descent stage and the fact that the QP used to obtain the spectrum vector was solved globally (see Table 4). Also, it can be seen that after about 40 iterations, the algorithm converged to a solution. From Figure 28(b), it can be seen that the step-size parameter γ changed values most dramatically at iterations

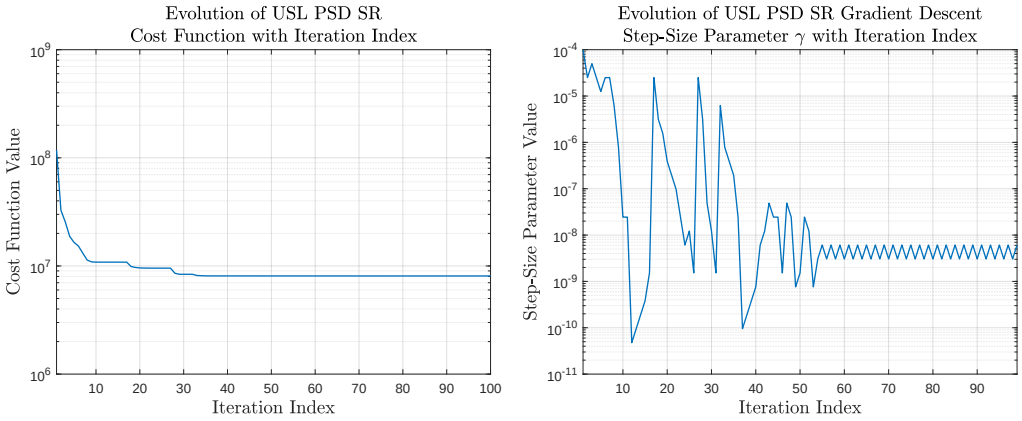

Figure 28. Evolution of the USL PSD SR algorithm with iteration index: (a) cost function $\xi(\mathbf{x}, \mathbf{s})$ from (30) and (b) step-size parameter γ from Sec. VII-B.1. ($N_{\text{iter}} = 100$, $\gamma_{\text{nom}} = 10^{-4}$, $c = 1/2$, $\tau = 1/2$.)

corresponding to abrupt changes in the objective function seen in Figure 28(a). This may suggest that the initial step-size value of 10^{-4} was overly large and that the algorithm may have jumped between local extrema before converging on one. When the algorithm finally converged, the step-size oscillated between 3-5 $\times$ 10^{-8}, corresponding to small values of γ.

It should be noted that the USL PSD SR algorithm required a much longer runtime than the USL TRP SR algorithm described in Sec. VI. This was due to the fact that solving the QP from (31) to get the spectrum vector $\mathbf{s}$ was much higher in computational complexity than solving the normal equations in (15) to get $\mathbf{s}_{\text{opt}}(\mathbf{x})$.

VIII. Concluding Remarks

Several of the pitfalls encountered with respect to solving the spectrum reconstruction problem for TES were brought to light in this article. In particular, the following issues made reconstructing spectra challenging:

- Ill-conditioning of the reconstruction problem due to nonuniform sampling near the Nyquist rate: This resulted in some samples being too close to one another, yielding overly correlated information, while other samples were too far apart from one another, resulting in missing information. It manifested in matrices used for reconstruction being effectively rank deficient.
- Discrepancies in the ICS mirror position outputs: Differences in OPD positions corresponding to fringe counts and the TES mirror motor encoder were on the order of 10^{-3} cm. Such values were large enough to correspond to vastly different values of the underlying IFGM waveform.
- Low resolution of the ICS measurements: Position data from the ICS was only output at a rate of 100 Hz, which was over an order of magnitude below the sample rate of the IFGM measurements (typically on the order of several kHz).

Interpolation was used to obtain positions in between the ICS measurements, but there is no guarantee that such an approach leads to accurate OPD values.

These matters are best exemplified in Figure 17. There we see the sensitivity of the spectrum reconstruction problem with respect to sample position errors, due in part to the fact that all IFGM waveforms relevant to TES are real, bandpass signals. As is evident from Figure 17, any errors in position locations could result in very different IFGM values. Conversely, IFGM values, such as those provided by the `SimCLK` module, can lead to highly erroneous spectra in the presence of OPD sample location errors.

These observations served as the impetus for investigating reconstruction algorithms which did not require explicit knowledge of the sample positions. The two most promising of such algorithms, which were described in this article, were the following:

- Unknown sample location (USL) Tikhonov regularized problem (TRP) spectrum reconstruction (SR): This algorithm sought to incorporate a priori knowledge of the spectrum to be reconstructed to better condition the reconstruction problem. The spectrum and position vectors were able to be jointly optimized locally using a gradient descent approach on the position vector.
- Unknown sample location (USL) power spectral density (PSD) spectrum reconstruction (SR): This algorithm sought to exploit the fact that all of the IFGM waveforms under consideration are inherently autocorrelation functions, in order to yield a more well-conditioned reconstruction problem. The spectrum and position vectors were alternately optimized by solving a convex quadratic programming (QP) problem to globally optimize the spectrum, followed by a gradient descent approach to locally optimize the position.

Unfortunately, neither of these algorithms were found to yield satisfactory reconstruction results, as evidenced in Secs. VI-D and VII-D. While both algorithms exhibited the behaviors that were expected, they both converged to local extrema that were far from the desired outcome. Furthermore, they resulted in OPD time series trajectories which appeared erratic in the neighborhood of the estimated ZPD location.

One avenue for future analysis would be to incorporate more sophisticated a priori information in the USL TRP SR algorithm. For example, using data collected when the TES laser was operational, desired spectrum mean/covariance values could be computed and used. Such an approach would be most appropriate for black-body (BB) spectra, which are known to be relatively stable across time and only vary slowly over the course of days [12]. With proper weighting, this could be used to infer OPD time series trajectories, which in turn could be used for reconstruction of target (TGT) and cold space (CS) spectra. Such reconstruction requires that the OPD time series does not evolve appreciably with time, which may be the case as suggested by the ICS data analysis carried out in Sec. IV.

---

[12] Ibid.

References

[1] E. Sarkissian and K. W. Bowman, "Application of a Nonuniform Spectral Resampling Transform in Fourier-Transform Spectrometry," *Applied Optics*, vol. 42, no. 6, pp. 1122–1131, Feb. 2003.

[2] P. P. Vaidyanathan, *Multirate Systems and Filter Banks*. Englewood Cliffs, NJ: Prentice Hall PTR, 1993.

[3] R. A. Horn and C. R. Johnson, *Matrix Analysis*, 2nd ed. New York, NY: Cambridge University Press, 2013.

[4] S. Boyd and L. Vandenberghe, *Convex Optimization*. New York, NY: Cambridge University Press, 2004.

[5] J. Browning, "Approximating Signals from Nonuniform Continuous Time Samples at Unknown Locations," *IEEE Trans. Signal Process.*, vol. 55, no. 4, pp. 1549–1554, Apr. 2007.

[6] M. Grant and S. Boyd, "CVX: MATLAB Software for Disciplined Convex Programming, version 2.1," http://cvxr.com/cvx, Mar. 2014.